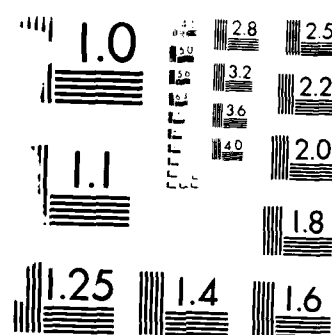


UNCLASSIFIED

ANALYSIS OF FIELD-WIDENED INTERFEROMETER DATA BY
LEAST-SQUARES AND SPECTRA. (U) UTAH STATE UNIV LOGAN
SPACE DYNAMICS LABS A S ZACHOR ET AL 31 MAY 85
SDL/85-033 AFGL-TR-85-0132 F19628-83-C-0056 F/G 4/1

狀

1111
1111
1111
1111



MICROCOPY RESOLUTION TEST CHART
NATIONAL BUREAU OF STANDARDS 1963 A

12

AFGL-TR-85-0132

ANALYSIS OF FIELD-WIDENED INTERFEROMETER DATA BY
LEAST-SQUARES AND SPECTRAL DECONVOLUTION METHODS

A. S. Zachor, R. D. Sharma, J. R. Winick and R. H. Picard

AD-A165 253

Atmospheric Radiation Consultants, Inc.
59 High Street
Acton MA 01720

The work reported herein was
performed under subcontract to
Space Dynamics Laboratories
Utah State University
Logan UT 84321

Editor: T. J. Gordon

Scientific Report No. 8

31 May 1985

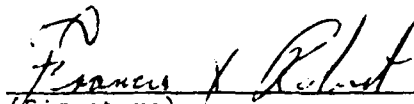
Approved for Public Release; Distribution Unlimited.

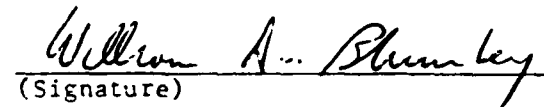
AIR FORCE GEOPHYSICS LABORATORY
AIR FORCE SYSTEMS COMMAND
UNITED STATES AIR FORCE
HANSCOM AIR FORCE BASE
MASSACHUSETTS 01731

OTIC FILE COPY

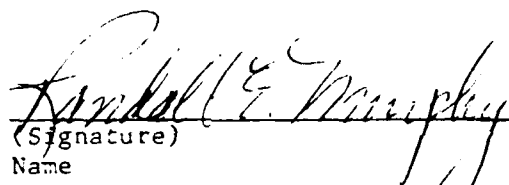
DTIC
*
10

"This technical report has been reviewed and is approved for publication"


(Signature)
FRANCIS X. ROBERT
Contract Manager


(Signature)
WILLIAM A. BLUMBERG
Branch Chief

FOR THE COMMANDER


(Signature)
Name
Division Director

This report has been reviewed by the ESD Public Affairs Office (PA) and is releasable to the National Technical Information Service (NTIS).

Qualified requestors may obtain additional copies from the Defense Technical Information Center. All others should apply to the National Technical Information Service.

If your address has changed, or if you wish to be removed from the mailing list, or if the addressee is no longer employed by your organization, please notify AFGL/DAA, Hanscom AFB, MA 01731. This will assist us in maintaining a current mailing list.

Unclassified

SECURITY CLASSIFICATION OF THIS PAGE

AD-A165253

REPORT DOCUMENTATION PAGE

1a. REPORT SECURITY CLASSIFICATION Unclassified		1b. RESTRICTIVE MARKINGS None	
2a. SECURITY CLASSIFICATION AUTHORITY		3. DISTRIBUTION/AVAILABILITY OF REPORT Approved for Public Release; Distribution Unlimited	
2b. DECLASSIFICATION/DOWNGRADING SCHEDULE			
4. PERFORMING ORGANIZATION REPORT NUMBER(S) SDL/85-033		5. MONITORING ORGANIZATION REPORT NUMBER(S) AFGL-TR-85-0132	
6a. NAME OF PERFORMING ORGANIZATION Space Dynamics Laboratories	6b. OFFICE SYMBOL (If applicable)	7a. NAME OF MONITORING ORGANIZATION Air Force Geophysics Laboratory	
6c. ADDRESS (City, State and ZIP Code) Utah State University Logan, Utah 84322-4140		7b. ADDRESS (City, State and ZIP Code) Hanscom Air Force Base, MA 01731	
8a. NAME OF FUNDING/SPONSORING ORGANIZATION Air Force Geophysics Laboratory	8b. OFFICE SYMBOL (If applicable) LSI	9. PROCUREMENT INSTRUMENT IDENTIFICATION NUMBER F19628-83-C-0056	
8c. ADDRESS (City, State and ZIP Code) Hanscom Air Force Base MA 01731 Contract Monitor: Francis X. Robert		10. SOURCE OF FUNDING NOS.	
		PROGRAM ELEMENT NO. 62101F	PROJECT NO. 7670
		TASK NO. 10	WORK UNIT NO. AK
11. TITLE (Include Security Classification) Analysis of Field-Widened Interferometer (OVER)			
12. PERSONAL AUTHOR(S) Zachor, A. S., Sharma, R. D., *Winick, J. R., *Picard, R. H., *			
13a. TYPE OF REPORT Scientific No. 8	13b. TIME COVERED FROM _____ TO _____	14. DATE OF REPORT (Yr., Mo., Day) 31 May 1985	15. PAGE COUNT 74
16. SUPPLEMENTARY NOTATION The work reported herein was performed under subcontract 84-051 to Space Dynamics Laboratories, Utah State University. Authors (*): AFGL, Hanscom AFB, MA 01731.			
17. COSATI CODES		18. SUBJECT TERMS (Continue on reverse if necessary and identify by block number)	
FIELD	GROUP	SUB. GR.	
		Interferometer data, least-squares analysis; spectral deconvolution; infrared; atmospheric emission; CO ₂ , NO ⁺ .	
19. ABSTRACT (Continue on reverse if necessary and identify by block number) Linear least-squares methods and the Jansson method of constrained nonlinear spectral deconvolution were used to analyze atmospheric emission spectra obtained in the Field-Widened Interferometer (FWI) experiment. The analysis provides estimates of line intensities and spectra of enhanced resolution. A conclusion of the study is that NO ⁺ was not present in the auroral event observed by the FWI.			
20. DISTRIBUTION/AVAILABILITY OF ABSTRACT UNCLASSIFIED/UNLIMITED <input checked="" type="checkbox"/> SAME AS RPT. <input type="checkbox"/> DTIC USERS <input type="checkbox"/>		21. ABSTRACT SECURITY CLASSIFICATION Unclassified	
22a. NAME OF RESPONSIBLE INDIVIDUAL Francis X. Robert, Contract Monitor, AFGL		22b. TELEPHONE NUMBER (Include Area Code) 617/861-3641	22c. OFFICE SYMBOL LSI

Unclassified

SECURITY CLASSIFICATION OF THIS PAGE

Block 11: Title (Continued)

Data by Least-Squares and Spectral Deconvolution Methods (UNCLASSIFIED)

Accession For	
NTIS AD-1	<input checked="" type="checkbox"/>
FOR	<input type="checkbox"/>
FOR	<input type="checkbox"/>

A-1

Unclassified

SECURITY CLASSIFICATION OF THIS PAGE

FOREWORD

For many years, the United States Air Force has supported experimental investigations into the chemistry and physics of upper atmospheric energy dynamics. In January 1983, to further this research, the Air Force Geophysics Laboratory (AFGL) awarded contract F19628-83-C-0056 to the Space Dynamics Laboratories (SDL) at Utah State University in Logan, Utah. This contract obligated SDL to design, build and operate certain field instruments whose goal was to measure the infrared spectral and spatial characteristics of upper atmospheric energy transfer, and to analyze the data these instruments recorded. As one step in satisfying this obligation, SDL designed and built a rocket-borne, field-widened interferometer (RBFWI) and, in April 1983, supported its launch aboard a Sergeant rocket (A30.276) from Poker Flat Research Range, Alaska, into a Class II aurora. The interferometer recorded significant auroral emission data in the infrared spectral region between 2.0 and 7.5 μm , from which researchers hoped to recover vertical profiles, time histories, densities and rotational/vibrational temperatures of certain atmospheric constituents.

Because of instrument effects inherent in the RBFWI, however, ordinary Fourier transform analysis of RBFWI interferograms cannot produce spectra of sufficient resolution to satisfactorily recover the desired information with standard spectral inversion processes. To overcome this problem, SDL sought the services of Atmospheric Radiation Consultants, Inc. (ARC), of Acton, MA, awarding them subcontract 84-051. Under this subcontract, ARC adapted two computer techniques to increase the resolution of the RBFWI spectra: a linear least-squares analysis and a nonlinear deconvolution algorithm. This publication describes the two methods and summarizes the results of their application to the RBFWI data. Unless otherwise noted, all the work reported herein was performed by the authors and ARC, Inc.

The authors are grateful for the generous support and encouragement of this project by Drs. Ken Schwartz and Peter Lunn of the Defense Nuclear Agency (DNA) and Drs. Don Ball and Ted Cress of AFSOR.

This Page Intentionally Left Blank

TABLE OF CONTENTS

	<u>Page</u>
Foreword	iii
Table of Contents	v
List of Figures	vii
List of Tables	ix
1. Introduction and Summary	1
2. Linear Least-Squares Analyses of FWI Spectra	7
2.1 Methods of Analysis	7
2.1.1 Estimation of Individual Line Intensities	7
2.1.2 Estimation of Band Contour Parameters	9
2.2 Apparatus Function for the FWI	15
2.3 Application to the ν_3 CO ₂ Band (2300-2380 cm ⁻¹ Region)	17
2.3.1 Individual Line Intensities	17
2.3.2 Band Contours	24
2.4 Application to the 2220-2300 cm ⁻¹ Region	32
3. Deconvolution Analysis of FWI Spectra	35
3.1 Background	35
3.2 Jansson's Method	36
3.3 Application to the ν_3 CO ₂ Band (2300-2380 cm ⁻¹ Region)	45
3.4 Application to the 2220-2300 cm ⁻¹ Region	53
References	63

This Page Intentionally Left Blank

LIST OF FIGURES

<u>Figure</u>	<u>Title</u>	<u>Page</u>
A	CO ₂ Line Intensities Inferred by Least Squares (Scan 10)	2
B	Deconvolved Segment of a Spectrum	3
1	The Contribution of the Line at $\nu=\nu_k$ to the Matrix Element G_{ij} . .	11
2	An Example of Partitions in Matrix Equations 8 and 9	13
3	¹² C ¹⁶ O ₂ Line Intensities Computed by Code NLTE	20
4	Comparison of Measured Spectrum for Scan 10 with Synthetic (NLTE) Spectrum of CO ₂ 00011-00001 lines	21
5	Line Intensities Inferred by Least-Squares and the Spectrum Reconstructed From These Estimates	22
6	Comparison of Residual Spectrum Errors with Inferred Line Intensities	24
7	Comparison of CO ₂ Line Intensities Obtained from Inferred Band Contour with Inferred NO ⁺ Line Intensities	28
8	Inferred Line Intensities for NO ⁺ 1-0 and 2-0 Bands	31
9	Comparison of Measured Spectrum from Scan 10 with Two Spectra Reconstructed from Inferred NO ⁺ band contours and line positions . .	33
10	Maximum Entropy Spectrum Computed for Scan 10	37
11	Comparison of Jansson's Relaxation Function (1984) with Relaxation Function Used in This Study	40
12	Image Spectrum of Sinc-Squared Lines and Deconvolved Spectra After 10 and 20 Iterations	44
13	Image Spectrum of Sinc-Squared Lines and Deconvolved Spectra After 20 Iterations, resolving lines 1.25 cm ⁻¹ Apart	46
14	Measured Spectrum for Scan 10 Convolved with Sinc-Squared Function to Effect Triangular Apodization	47
15	Illustration of Results of Deconvolving Scan 10 Spectrum	48
16	Illustration of Deconvolved Scan 10 Spectrum (Expanded Scale) . .	50
17	Illustration of Deconvolved Scan 6 Spectrum (Expanded Scale) . . .	51
18	Deconvolved Scan 10, 2390-2330 cm ⁻¹ Region	52
19	Comparison of Deconvolved Spectra from scans 6 and 10	54

LIST OF FIGURES

<u>Figure</u>	<u>Title</u>	<u>Page</u>
20	Spectra Computed by USU from Hamming-apodized Interferogram . . .	55
21	Deconvolved Spectrum for Scan 8	57
22	Deconvolved Spectrum for Scan 6	58
23	Deconvolved Spectrum for Scan 2.	59
24	Deconvolved Spectrum for Coadded scans 2, 3 and 4	60
25	Positions of NO^+ in 2220-2300 cm^{-1} Region	61

LIST OF TABLES

<u>Table</u>	<u>Title</u>	<u>Page</u>
1	The Five Strongest $^{12}\text{C}^{16}\text{O}_2$ Transitions for the 2300-2380 cm^{-1} Spectral Region	19
2	CO_2 (00011-00001) Line Positions and Intensities	26
3	CO_2 Line Intensities Inferred by Band Contours Least-Square Method	30

This Page Intentionally Left Blank

SECTION 1

INTRODUCTION AND SUMMARY

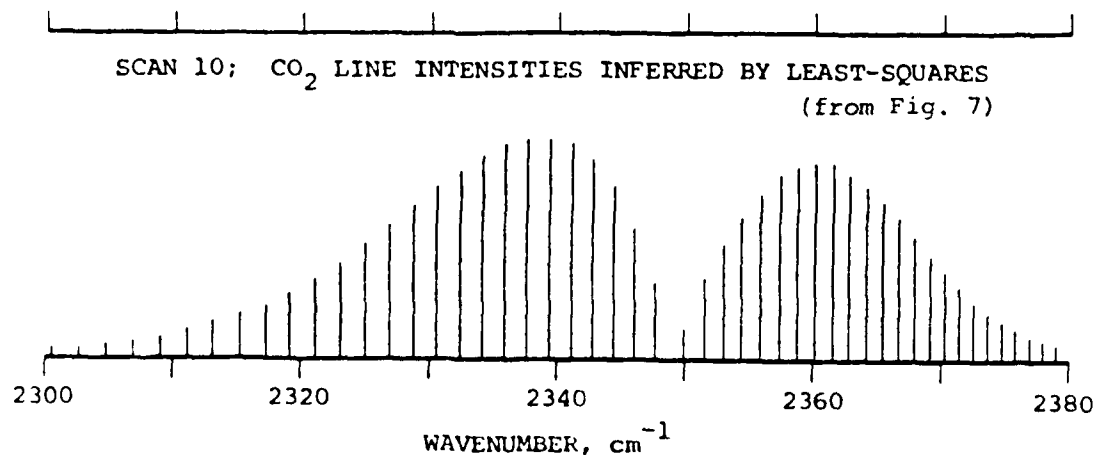
The Field-Widened Interferometer (FWI) is a cryogenically-cooled, rapid-scan Michelson interferometer spectrometer with special field compensation, designed to measure auroral emissions between 2 and 7.5 μm wavelength at $\sim 1.1 \text{ cm}^{-1}$ resolution (unapodized). It was launched aboard a Sergeant rocket in April, 1983 from Poker Flat, Alaska into an IBC Class II aurora. In this experiment, sponsored by the Defense Nuclear Agency and the Air Force Geophysics Laboratory, the uplooking instrument obtained interferograms every 1.5 seconds from 86 km altitude up to 139 km (flight apogee), and down to 60 km altitude on descent. Details of the instrumentation and experiment, and examples of the excellent spectra obtained, are given by Steed, et al (1983).

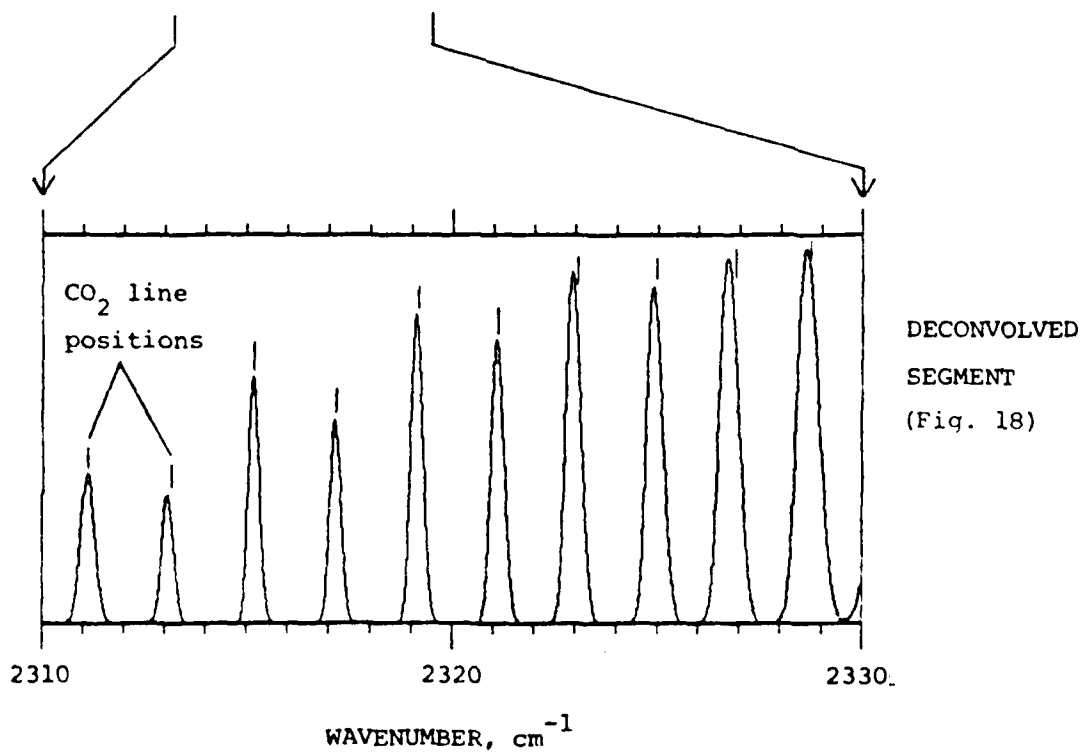
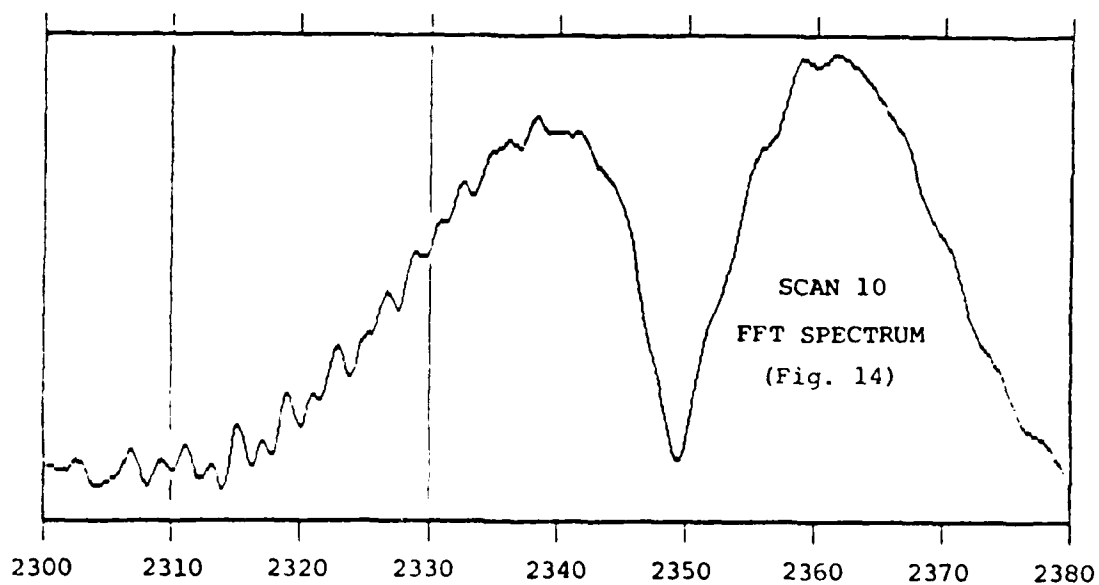
It is planned to analyze spectra from the FWI experiment by an inversion process that will recover vertical profiles and possibly time histories of the translational temperature, CO_2 and NO excited state densities and the CO_2 ν_3 vibrational temperature. The method that will be used, a modification of the limb inversion technique developed by Zachor and Sharma (1985), requires the use of individual lines (or narrow spectral regions) of differing opacities, including optically thin lines. The FWI spectra of 1.1 cm^{-1} resolution do not provide adequate spectral isolation because of the strong sidelobes in the apparatus function corresponding to this resolution. Suppression of the sidelobes by apodization of the interferograms degrades the resolution to $\sim 2.2 \text{ cm}^{-1}$, which is not sufficient to resolve the CO_2 lines. Thus, the inversion technique cannot be implemented until the existing FWI spectra are a.) analyzed to obtain estimates of individual line intensities or b.) are recomputed by a method that yields higher spectral resolution (i.e., higher than is provided by Fourier analysis of the interferograms).

The primary purpose of the present study was to set in place procedures and computer codes for performing both types of spectral estimation. Straightforward linear least-squares methods were adapted for the determination of line intensities. For resolution enhancement we selected the constrained nonlinear deconvolution algorithm of Jansson (1984). A second objective was to determine, by these techniques, whether ionized nitric oxide (NO^+) was present in the auroral event observed by the FWI.

Sections 2 and 3 describe the methods and results of their application to FWI data for two spectral regions: the $2300\text{--}2380\text{ cm}^{-1}$ region which spans the strong ν_3 band of CO_2 , and the $2220\text{--}2300\text{ cm}^{-1}$ region in which NO^+ would probably be the dominant radiator, if present. The methods are fairly general and can be applied to data that will be obtained in forthcoming AFGL/DNA experiments, including HIRAM, SPIRIT and CIRRI 1A.

The figures below are examples of results obtained for the $2300\text{--}2380\text{ cm}^{-1}$ region from FWI scan 10, measured at $\sim 101\text{ km}$ altitude. The first figure shows, as a stick spectrum, the intensities of the CO_2 lines inferred by least-squares with the constraint that the intensities follow a smooth band contour. This display is, for all intents





and purposes, an infinitely resolved spectrum of the source (even the Doppler line shape has been eliminated). The least-squares approach requires knowledge or recognition of the radiators present and the positions of their spectral lines. When this prior information is available, the method is both the simplest and most effective of the various techniques available for "superresolved" spectral recovery. We describe in this report a least-squares method that is applicable even when overlapping bands result in coincident and near-coincident lines.

The second figure shows the spectrum obtained by conventional FFT analysis of the triangularly apodized scan 10 interferogram, and a section of this spectrum after deconvolution by the Jansson algorithm. The apodization is necessary because the Jansson method is effective only if the apparatus function is positive definite. The full width at half maximum (FWHM) of the lines in the deconvolved spectrum is $\sim 0.5 \text{ cm}^{-1}$, which is 4.4 times better than the $\sim 2.2 \text{ cm}^{-1}$ resolution of the starting spectrum (or 2.2 times better than the 1.1 cm^{-1} resolution for the unapodized case). Moreover, the positions of these CO_2 lines are correct to within $\sim 0.2 \text{ cm}^{-1}$ and there are no sidelobes. The achieved resolution enhancement is much less in the R branch of the CO_2 band where the lines are more closely spaced. Included in Section 3 is a spectrum recovered for scan 10 by the Maximum Entropy Method (MEM). The MEM gave somewhat greater resolution enhancement but did not accurately reproduce the CO_2 line positions.

Five lines of the NO^+ 1-0 band (P4 through P8) and four lines of the 2-1 band (R0 through R3) fall between 2310 cm^{-1} and 2330 cm^{-1} , but none of these appear in the deconvolved spectrum segment. Similarly, none of the many lines of the 2-1 through 6-5 bands that occur between 2220 and 2300 cm^{-1} were found in the deconvolved FWI spectra for this region (with just a few exceptions noted in Section 3.4). It is concluded that NO^+ was not observed in the FWI experiment. There are many emission features between 2220 and 2300 cm^{-1} in the deconvolved spectra, but these could not be identified with any common atmospheric species such as $\text{C}^{13}\text{O}_2^{16}$, N_2O and O_3 that radiate in

this region. The emission features also change markedly from scan to scan, indicating that the observed source was changing rapidly, or perhaps that these features are instrumental artifacts.

The two analysis methods described and implemented in this study require knowledge of the instrumental line shape or apparatus function. Since it was not determined during calibration, we assumed it to be the usual sinc function (for the unapodized case). It is recommended that the apparatus function be measured in future programs.

The FWI experiment included ground-based observations of the auroral event, on-board photometer measurements at 3914Å and 5577Å, and on-board (in situ) measurements of oxygen atom density. These data were not available to us and hence could not be used in interpreting the measured radiance spectra.

In summary, the reported effort demonstrates the remarkable super-resolution capabilities of least squares analysis and the Jansson deconvolution method. Application of these methods to the FWI data base leaves unresolved an important question, apart from the identification of a radiator(s) in the $2220\text{--}2230\text{ cm}^{-1}$ region: Why do the CO_2 lines in the red wing of the P-branch seem alternately too strong or too weak, whether resolved by least-squares (without a smoothness constraint) or by the Jansson method? This behavior is seen in the second figure above. Vibrationally excited CO_2 is produced by energy transfer during collisions with N_2 . Since the radiative lifetime of the ν_3 mode is so short (~ 2 msec), the excited CO_2 molecules at these altitudes (~ 100 km) are probably not thermalized before radiating. The observed rotational distribution is that of the nascent molecules which may not be Maxwell-Boltzmann. The observed distribution is intriguing but as yet we have no explanation for it.

(THIS PAGE INTENTIONALLY LEFT BLANK.)

SECTION 2

LINEAR LEAST-SQUARES ANALYSES OF FWI SPECTRA

2.1 Methods of Analysis

Two methods will be described that estimate the intensities of lines in a measured spectrum. It is assumed that the positions of lines that may be present are known to high accuracy, and that the apparatus function of the spectrometer is known. One of the methods solves directly for the individual intensities. The other solves for a set of coefficients that define the band spectral contour, or several contours if it is known that there are overlapping bands in the spectrum. These coefficients and the line positions can then be used to estimate the line intensities.

The number of solutions sought in either method is always smaller (usually much smaller) than the number of spectrum points available. That is, the solutions give best estimates in the overdetermined least-squares sense. The methods are linear and are therefore easily implemented on the computer.

2.1.1 Estimation of Individual Line Intensities

Let L_{ij} denote the spectral radiance that the instrument would measure at wavenumber ν_i for a single, very narrow line source of wavenumber ν_j . In other words, L_{ij} is a shift-variant apparatus function if it depends on both ν_i and ν_j , as is the case for the FWI. In the more usual shift-invariant case, L_{ij} depends on only $\nu_i - \nu_j$. Except when specifically defined, L_{ij} can represent either case; this will be true also in the equations of Section 3 that define the Jansson deconvolution algorithm.

The source emission lines in the FWI experiment are much narrower than the apparatus function, and for our purposes can be regarded as an array of delta functions, i.e., as a "stick spectrum". The corresponding measured spectrum can be written

$$S(v_i) = \sum_{j=1}^N L_{ij} a_j; \quad i = 1, 2, \dots, M, \quad (1)$$

where the a_j are the unknown intensities of the lines at spectral locations v_j , N is the number of lines and M is the number of points comprising the measured spectrum ($M > N$). In matrix notation this equation is

$$\underline{S} = \underline{L} \underline{a}. \quad (2)$$

Given the measured spectrum (column vector \underline{S}) and the line shape matrix \underline{L} , one can obtain an estimate \underline{a}' of the true line intensity vector \underline{a} . A well-known least-squares solution (one that minimizes the variance between \underline{S} and $\underline{L}\underline{a}'$) is

$$\underline{a}' = \left[\underline{L}^T \underline{L} + \alpha \underline{I} \right]^{-1} \underline{L}^T \underline{S}, \quad (3)$$

where $()^T$ and $()^{-1}$ denote matrix transpose and inverse, and \underline{I} is the N by N identity matrix. The term $\alpha \underline{I}$ has the effect of suppressing contributions to \underline{a}' by eigenvectors of $\underline{L}^T \underline{L}$ with small eigenvalues, i.e., of suppressing possible instability arising from noise in \underline{S} . An appropriate value for α if the system noise-equivalent spectral radiance (NESR) is known is

$$\alpha = (\text{NESR})^2 / \text{variance of } \underline{S}. \quad (4)$$

Equation 3 is useful for estimating individual line intensities when the lines are well separated. Lines may be coincident or nearly so when the spectral region under consideration contains two or more overlapping bands (bands of different species or different subbands of a single species). Obviously, lines that are exactly coincident must be treated as a single line; one can estimate only their summed intensities. Equation (3) will give poor results when line separations occur that are small compared to the instrument average spectral resolution Δv .

2.1.2 Estimation of Band Contour Parameters

Band "contour" refers here to the smooth function or envelope describing the variation of intensity from line to line within a molecular band. Spectral lines that are nearly coincident will usually belong to different bands, and it is unlikely that the different band contours will be coincident (or proportional to one another) over an appreciable fraction of the band widths. These properties of overlapping bands and knowledge of the line positions make it possible to solve for the band contours, and then, as a second step, for the individual line intensities. If the contours are represented as weighted sums of basis functions, the problem remains linear and the initial solution gives estimates of the weights. This solution can be cast in the form of Eq. (3), as will be demonstrated.

For later convenience we change the summation index in Eq. (1) from j to k to obtain

$$S(v_i) = \sum_k L_{ik} a_k ; \quad i = 1, 2, \dots, M . \quad (5)$$

Again, $S(v_i)$ are the measured spectrum points. The a_k are the unknown intensities of lines at the known positions v_k . If the lines belong to a single band, the a_k can be regarded as samples of a continuous contour or envelope intensity function $E(v)$, which, in turn, can be represented by a weighted sum of continuous basis functions $F_j(v)$:

$$a_k = E(v_k) \equiv \sum_j c_j F_j(v_k) , \quad (6)$$

where the c_j are the weights (the new unknowns). The result of substituting Eq. (6) into Eq. (5) and changing the order of summation is

$$S(v_i) = \sum_j \left[\sum_k L_{ik} F_j(v_k) \right] c_j . \quad (7)$$

This is the same as

$$S(v_i) = \sum_{j=1}^N G_{ij} c_j ; \quad i = 1, 2, \dots, M , \quad (8)$$

if

$$G_{ij} \equiv \sum_{k'} L_{ik} F_j(v_k) . \quad (9)$$

Equation (8) has the same form as Eq. (1). Thus, a least-squares estimate of the N weights c_j is given by Eq. (3) after appropriate changes in notation:

$$\underline{c}' = \left[G^T G + \alpha I \right]^{-1} G^T \underline{S} . \quad (10)$$

The matrix element G_{ij} , in physical terms, is the total spectral radiance at v_i due to all source lines of a given band, but whose intensities include only the j th component (basis function) of the band contour. The contribution of a typical line, which corresponds to a single term in the right hand side of Eq. (9), is pictured in Figure 1.

The application of these results consists of the following steps: First, choose a set of basis functions $F_j(v)$ capable of representing a typical band contour. Then, from the given line positions v_k and matrix elements L_{ik} , compute matrix G using Eq. (9). Solve for vector \underline{c}' using Eq. (10), and finally for the line intensities using Eq. (6).

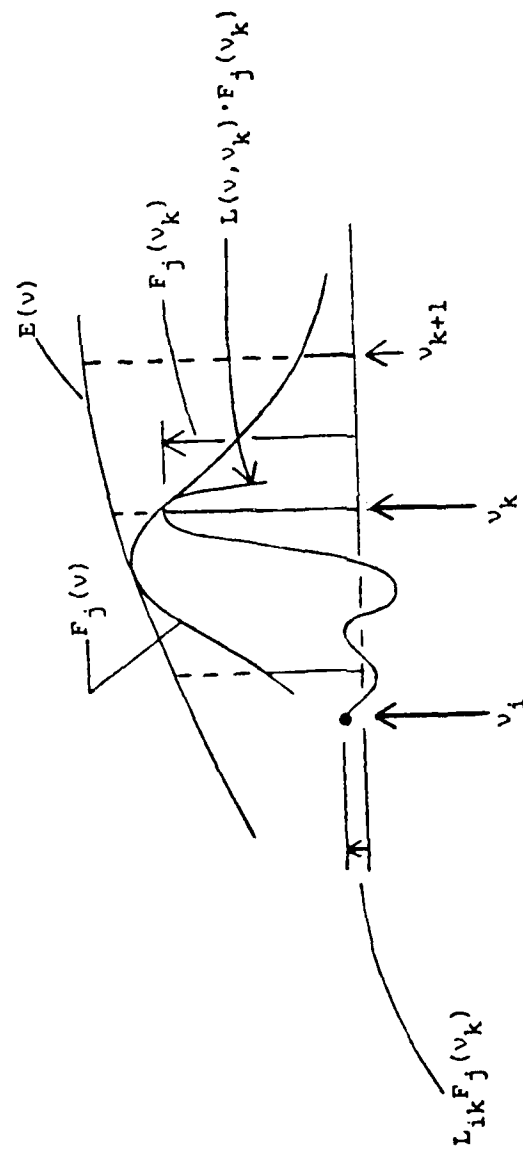


Figure 1. The contribution of the line at $\nu = \nu_k$ to the matrix element G_{ij} .

The discussion of the method thus far implies that the lines belong to a single band, i.e., that there are no additional, overlapping bands. Indeed, the present method may be preferable to the one described in Section 2.1.1 in the non-overlapping case since it (the present method) imposes the constraint that the estimated line intensities follow a smooth contour. The choice would depend on available signal-to-noise and the flexibility of the selected basis functions; a smoothness overconstraint is obviously undesirable.

The method of solution described in this section is made applicable to the case of overlapping bands by generalizing the definitions of matrices L and G . Note that subscript k refers always to a particular line and thus implies a particular band. For example, $k = 1$ to 25 might represent the lines of band A and $k = 26$ to 100 the lines of band B. Similarly, j refers to a particular basis function associated with a particular band; $j = 1$ to 3 might represent the basis functions for band A and $j = 4$ a single basis function used for band B. In other words, multiple bands may be accommodated by one or more partitions along the columns of L and G . The column partitions in G correspond to row partitions in the column vectors \underline{c} and \underline{c}' . Figure 2 shows the partitions in G , \underline{c} and L for the present example, as well as the corresponding column/row partitions in $F \equiv [F_{kj}]$, representing the basis function samples $F_j(v_k)$. The figure also illustrates the evaluation of Eqs. (8) and (9). Note that certain combinations of j and k are not allowed (are zero) in matrix F . Thus, the summation indices in Eqs. (6) and (9), which both involve F , are restricted to certain values. Equations (8) and (10) are evaluated in the normal manner; i.e., the partitions serve merely to label groups of vector or matrix elements. The labels are needed in Eq. (10) only for the solution vector \underline{c}' so that its elements can be assigned to the proper band, and so that the estimated line intensities for each band can then be correctly obtained via Eq. (6).

We conclude this subsection with a general description of the basis functions that were used in analyzing FWI spectra. Note that the equations

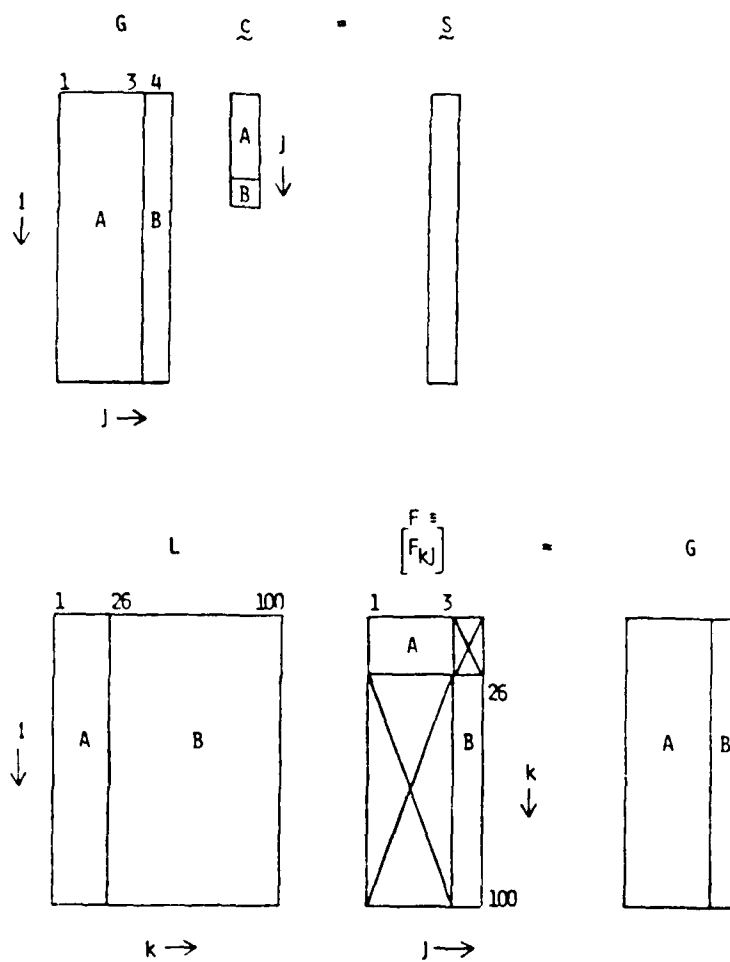


Figure 2. An example of partitions in the matrix equations $Gc = S$ (Eq. 8) and $LF = G$ (Eq. 9).

require only the values $F_j(v_k)$, equal to the basis functions evaluated at known line frequencies v_k . A particular v_k implies a particular band, a branch of that band (P, Q or R), and a rotational quantum number J . The contours of P branches were represented by the bases

$$F_j(v_k) = J \exp[-\alpha_j J(J+1)] , \quad (11)$$

where J has the value implied by v_k , and the α_j are selected from the set of values

$$\left[J_j (2 J_j + 1) \right]^{-1} \quad (11a)$$

determined by the set J_j . Equation (11) approximates the theoretical distribution of line intensities for a typical P-branch for a given rotational temperature (proportional to $1/\alpha_j$). It increases initially with J (or corresponding distance between v_k and the band origin), reaches a maximum, and then falls off with a long, exponential-like tail. The maximum occurs at $J = J_j$. One might, for example, choose to use three basis functions whose α_j 's are given by Eq. (11a) with $J_j = 6, 10$ and 14 . A weighted sum of these basis functions, representing the P branch contour, will peak anywhere between approximately 6 and 14 depending on the relative weights.

Similarly, the contours of R branches were represented by the bases

$$F_j(v_k) = (J+1) \exp[-\alpha_j J(J+1)] . \quad (12)$$

The α_j were selected from

$$\left[(J_j + 1) (2 J_j + 1) \right]^{-1} \quad (12a)$$

to obtain maxima at the $J = J_j$.

A single set of J_j 's was used for the P and R branches of the same band, but separate solutions (basis function weights) were obtained for the two branches. There were no strong Q branches in the FWI spectra analyzed by this method.

2.2 Apparatus Function for the FWI

The shift-variant apparatus function L_{ij} must be known in order to apply the least squares methods described above or to apply the deconvolution technique described in Section 3. Recall that $L_{ij} \equiv L(v_i, v_j)$ is defined as the spectral radiance at wavenumber v_i due to a discrete line source of wavenumber v_j . The interferograms obtained by the FWI consist of a set of samples corresponding to equal increments in the lateral displacement of a field-widening wedge, or, equivalently, to equal increments in optical retardation x at some reference wavenumber. Taking the Fourier transform of whatever truncation/apodization function is applied to the interferogram yields a basic shift-invariant apparatus function $L(\sigma_i, \sigma_j)$, where σ is the variable conjugate to the sampling retardation variable x . Conservation of energy (line intensities) requires that

$$L(v_i, v_j) dv_i = L(\sigma_i, \sigma_j) d\sigma_i, \quad (13)$$

i.e., the integrals over the two sides must be equal. Note that v is some (nonlinear) function of σ (or σ a function of v) because the index of refraction of the wedge material varies with wavelength. Thus, if $L(\sigma_i, \sigma_j)$ is known, the desired apparatus function $L_{ij} \equiv L(v_i, v_j)$ can be obtained from

$$L_{ij} = L[\sigma(v_i), \sigma(v_j)] (d\sigma/dv)_{v=v_i}. \quad (14)$$

The function $\sigma(v)$ and its derivative $d\sigma/dv$ were determined by USU during calibration of the FWI and have been provided as FORTRAN function subroutines GFUNC(v) and GDERV(v), respectively:

$$\begin{aligned}\sigma(v) &\equiv \text{GFUNC}(v) \cdot F \\ d\sigma/dv &\equiv \text{GDERV}(v) \cdot F \\ F &\equiv 5 \times 632800 \times 65536 \times 10^{-10} \\ v &\text{ given in cm}^{-1}\end{aligned}\tag{15}$$

The two subroutines are listed below.

```

      FUNCTION GFUNC(W)
C
C*   USED IN CALCULATING THE DISTORTED FWI LINESHAPE
C
      PARAMETER( COEF1=+.10252946 )
      PARAMETER( COEF2=-.15787537E5 )
      PARAMETER( COEF3=-.21755914 E10 )
      PARAMETER( COEF4=+.34318074E-11 )
      WW = W*W
      GFUNC = W*(COEF1 + (COEF2 + COEF3/WW)/WW + COEF4*WW)
      RETURN
      END

C
C
C
C
C
      FUNCTION GDERV(W)
      PARAMETER( COEF1=+.10252946 )
      PARAMETER( COEF2=-.15787537E5 )
      PARAMETER( COEF3=-.21755914E10 )
      PARAMETER( COEF4=+.34318074E-11 )
      WW = W*W
      GDERV = COEF1 - (COEF2 + 3.*COEF3/WW)/WW + 3.*COEF4*WW
      RETURN
      END

```

The least-squares analysis methods were applied to spectra computed by USU from unapodized interferograms of length $64K = 65536$. For this

case the apparatus function in the σ -space is

$$L[\sigma(v_i), \sigma(v_j)] = \frac{\sin \pi [\sigma(v_i) - \sigma(v_j)] / \Delta \sigma}{\pi [\sigma(v_i) - \sigma(v_j)]} \quad (16)$$

with $\Delta \sigma = 2.0$. The corresponding wavenumber resolution $\Delta \nu = \Delta \sigma \cdot (d\sigma/d\nu)^{-1}$, where the derivative is given by Eq. (15), is $\sim 1.0 \text{ cm}^{-1}$ ($\sim 0.91 \text{ cm}^{-1}$ to first sinc zero and $\sim 1.1 \text{ cm}^{-1}$ FWHM).

The FWI spectra in the region $2200\text{--}2320 \text{ cm}^{-1}$ change markedly from scan to scan over certain portions of the flight, indicating that the observed column thickness of the radiating species (NO^+ ?) is changing due to the motion of the rocket, and/or that local properties within the column above the rocket are changing rapidly with time. In order to represent the effects of a "changing source" in a simplified parametric manner, we assume that all spectral components of the source change according to a single multiplicative function of time. This is the same as saying the effects can be represented by applying a single apodization function to the interferogram. We assume that this function is an exponential and characterize it by its value c at maximum retardation, which is also the ratio of apparent source intensity at maximum retardation to that at zero retardation. This parameter may be varied to obtain maximum agreement between the measured spectrum and one reconstructed from the inferred line intensities. Note that c can be greater than unity for source intensity decreasing with time, since the maximum retardation signal is measured before the zero retardation signal during even numbered scans.

For the exponentially varying source, the basic sinc function instrument line shape of Eq. (16) is replaced by

$$(1/\Delta \sigma) \left\{ \ln c [c \cos q - 1] + c q \sin q \right\} \div [(\ln c)^2 + q^2] \quad (17)$$

where $q \equiv \pi[\sigma(v_i) - \sigma(v_j)]/\Delta\sigma$. Equation (17) reduces to the sinc function for $c \rightarrow 1$.

2.3 Application to the ν_3 CO₂ Band (2300-2380 cm⁻¹ region)

The two methods described above were applied to the spectral region 2300-2380 cm⁻¹ of FWI scan No. 10, which was obtained at ~ 101 km altitude during the upleg portion of the flight. There are some half-dozen overlapping bands of C¹²O₂¹⁶ in this region, and it was necessary to decide which CO₂ bands/lines to include in the analysis. To this end, theoretical or "expected" line intensities were computed using AFGL's code NLTE [see Sharma et al (1983)], which had just been modified to handle the zenith viewing geometry of the FWI experiment in addition to the limb viewing geometry.

The five strongest bands of C¹²O₂¹⁶ for this region, in order of decreasing band intensity at temperature 298K, are listed in Table 1. The band origins and lower state energies are taken from the current AFGL line parameters compilation [Rothman, et al (1983)]. The NLTE computations are based on assumed temperature, pressure, and CO₂ density profiles, and an estimated ν_3 vibrational temperature profile provided by J. Kumer of Lockheed to R. Sharma of AFGL. The "observer" altitude was taken as 100 km. The stick spectrum of Fig. 3 shows the computed zenith-view intensities of all lines of the five CO₂ transitions for the spectral region 2300-2390 cm⁻¹. Lines whose apparent intensities are less than the vertical resolution of the plot (the thickness of the baseline axis) are plotted as sticks of height equal to twice this resolution. Only the two strongest bands have definable contours in the figure.

2.3.1 Individual Line Intensities

It was decided to apply the method of Section 2.1.1 to the lines of the strongest transition. Note that the maximum line intensity for the

Table 1. The Five Strongest $C^{12}O_2^{16}$ Transitions for the
2300-2380 cm^{-1} Region [see Rothman, et al (1983)]

Band Origin (cm^{-1})	Band		Lower State Energy (cm^{-1})
	v'	v''	
2349.143	00011	00001	0.
2336.633	01111	01101	667.379
2324.141	02211	02201	1335.129
2327.433	10012	10002	1285.4087
2326.598	10011	10001	1388.1847

next weaker transition (the strongest hot band) is only seven percent of that for the included lines. Lines and data outside the region 2300-2381.75 cm^{-1} were discarded; this resulted in a total of $N = 52$ lines of CO_2 (00011-00001) and $M = 328$ measured spectrum values. In this first analysis we also ignored the possibility that overlapping bands of NO^+ were present in the measured spectrum. The apodization parameter c was set to unity, corresponding to a constant source.

The theoretical stick spectrum of Fig. 3, but including only the CO_2 lines whose positions were used in the analysis, is reproduced in the lower part of Figure 4. The upper part of the figure shows the USU measured spectrum for scan 10. Note that there are negative amplitudes due to sidelobes in the phase-corrected USU spectrum. Note also that the predicted CO_2 line positions, which are indicated by hash marks, do not coincide with the spectrum peaks except near $v \approx 2320$ cm^{-1} ; i.e., sidelobes contribute as much to spectral structure as the central lobes throughout most of the spectrum.

Figure 5 shows the results of the least-squares analysis. The inferred line intensities are displayed as a stick spectrum in the lower part of

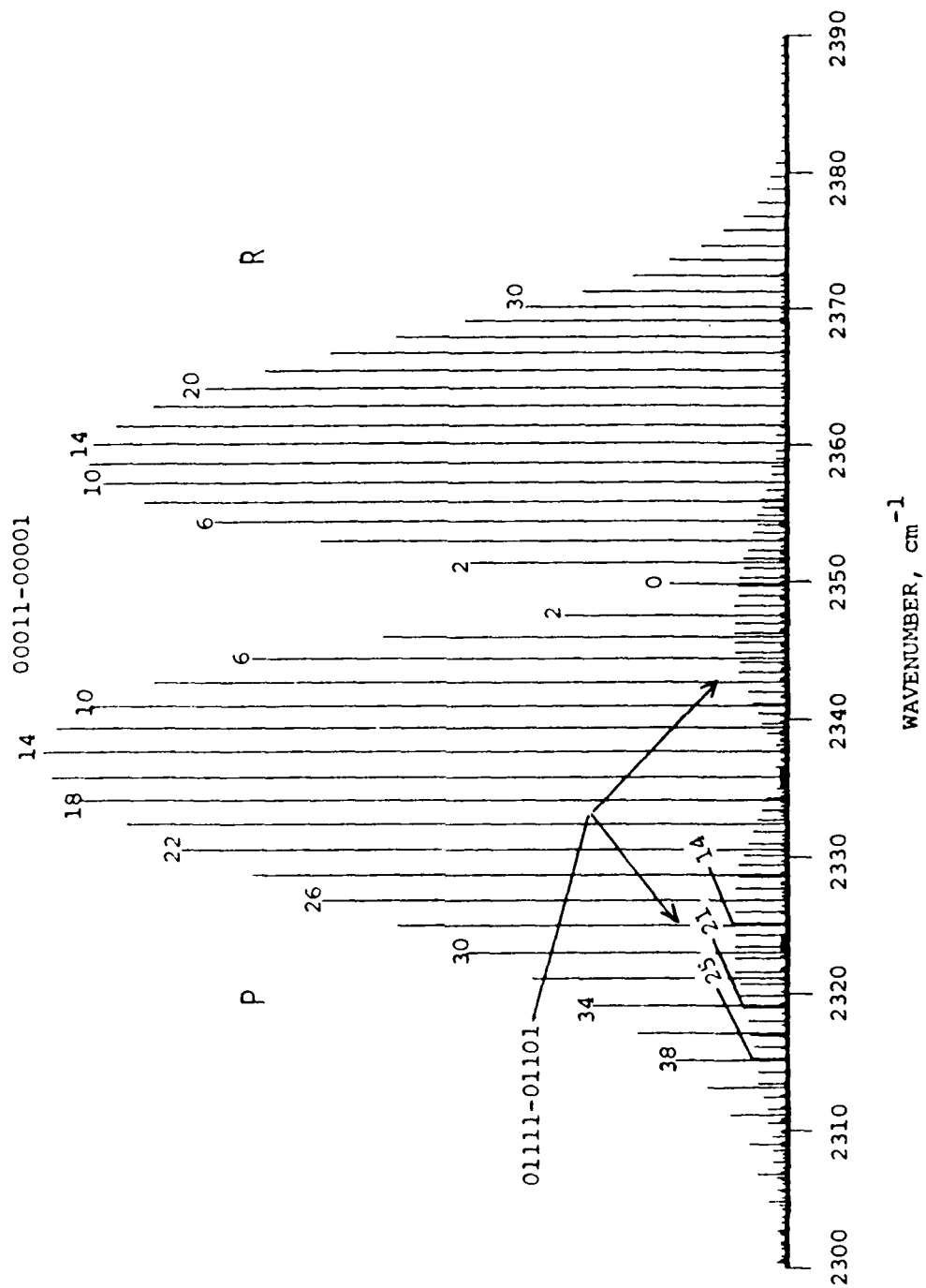


Figure 3. $^{12}\text{O}^{16}\text{O}_2$ line intensities computed by code NLTE.

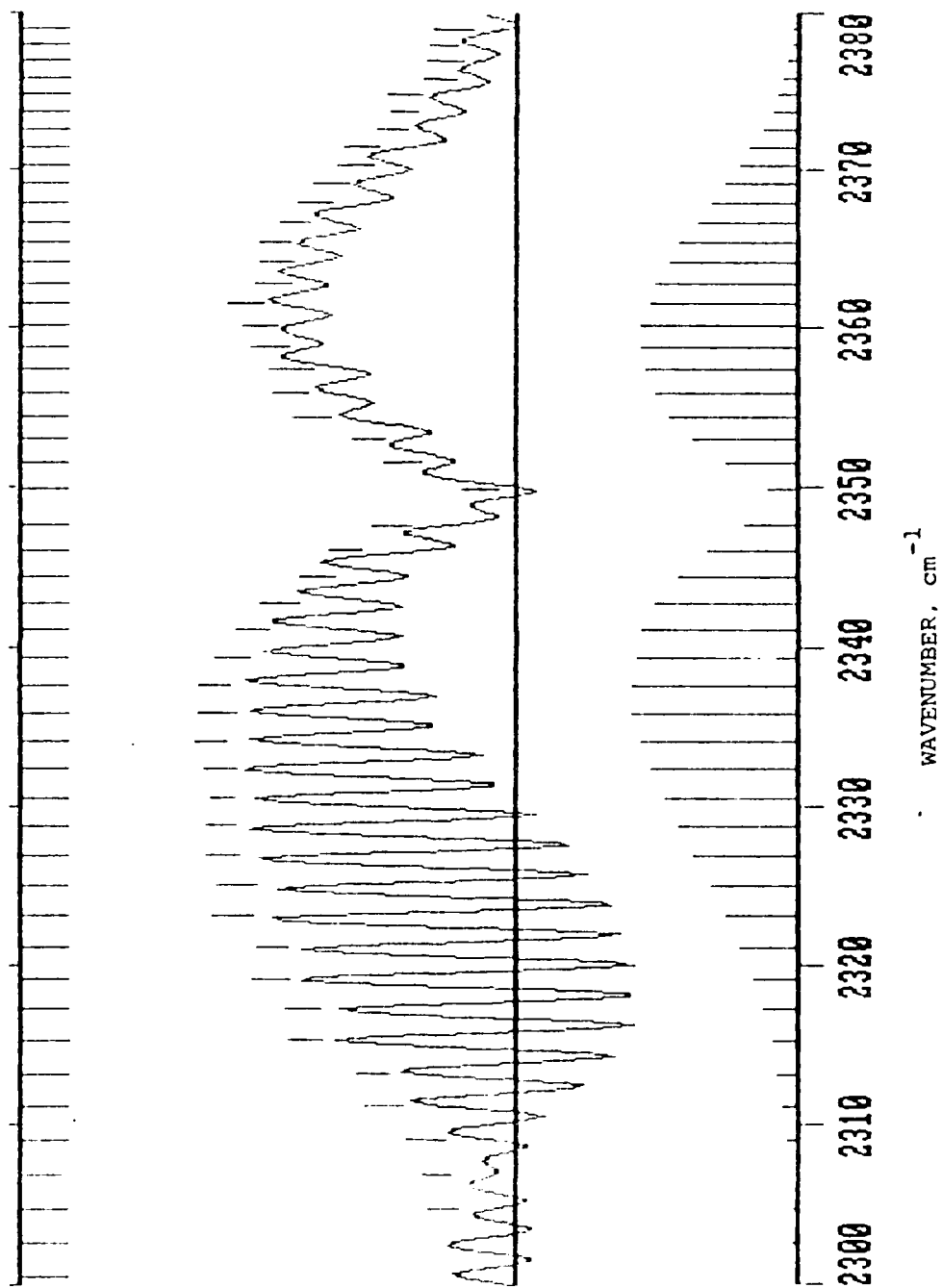


Figure 4. Upper section: Measured spectrum for scan 10.
Lower section: Synthetic (NLTE) spectrum of CO₂ 00011-00001 lines.

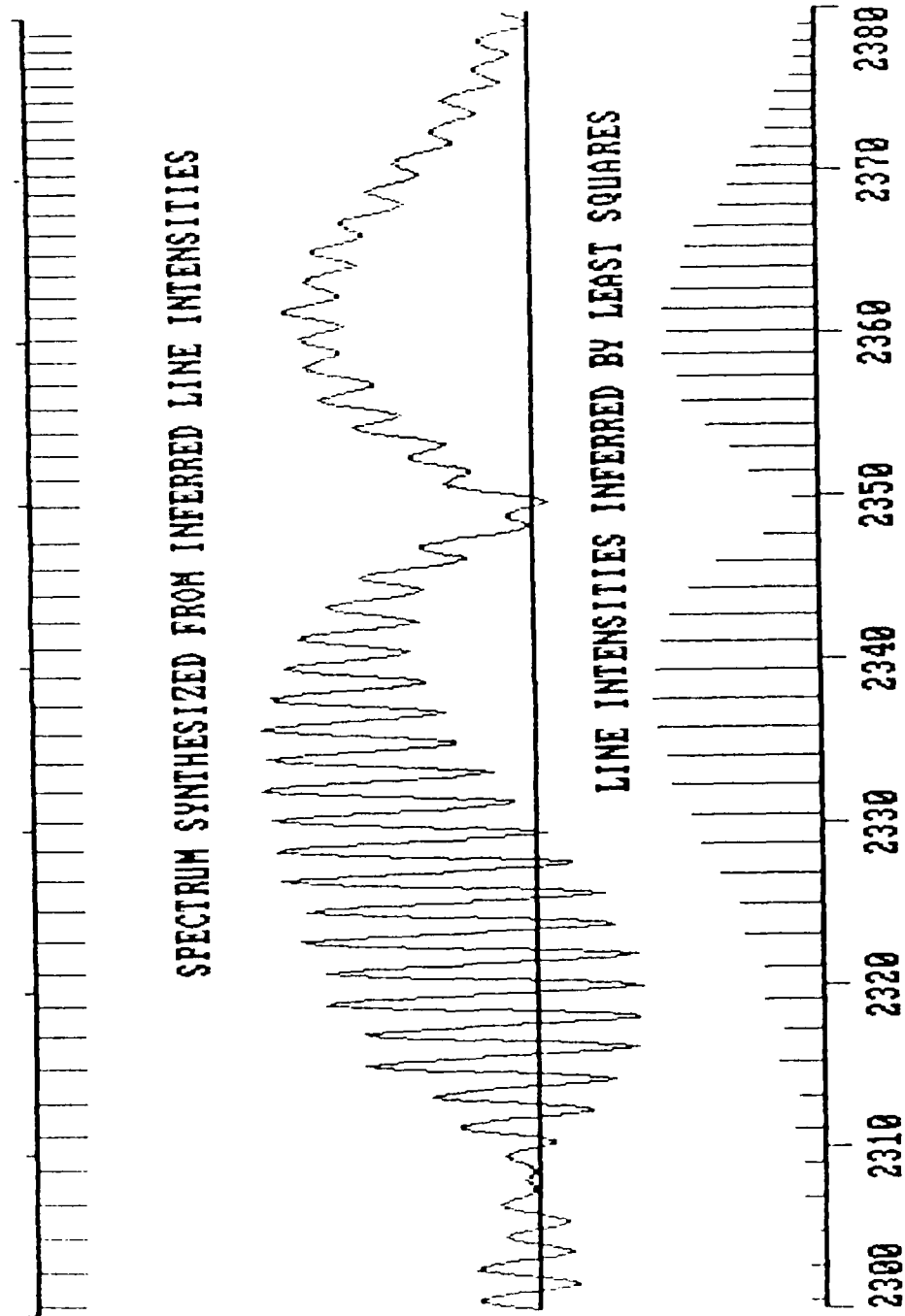


Figure 5. Line intensities inferred by least-squares and the spectrum reconstructed from these estimates.

the figure, and the spectrum synthesized (reconstructed) from the intensity estimates is shown in the upper part.* The least-squares process has minimized the variance between this reconstructed spectrum and the measured one. Figure 6 shows the inferred line intensities again, and also the difference between the reconstructed spectrum and the measured one. The rms of this difference spectrum is only four percent of the maximum measured spectral radiance; the maximum difference, which occurs near $\nu = 2310 \text{ cm}^{-1}$, is 13 percent of the maximum measured spectral radiance.

The maximum spectral radiance in the measured spectrum (Fig. 4, upper curve) is $8.9 \times 10^{-11} \text{ W/cm}^2 \text{ sr cm}^{-1}$. This value corresponds to a maximum signal-to-noise ratio of 445 based on the NESR of $2 \times 10^{-13} \text{ W/cm}^2 \text{ sr cm}^{-1}$ (at $5 \text{ }\mu\text{m}$ wavelength) quoted by Cook, et al (1984) for the FWI. The noise-to-signal power, denoted by α in Eqs. (3) and (4), was found to be $\sim 5 \times 10^{-5}$; α must have had virtually no effect in the solution (Eq. 3) since the diagonal elements of $L^T L$ were of order 10.

The inferred line intensities (Fig. 5) define a reasonably smooth band contour at wavenumbers larger than $\sim 2325 \text{ cm}^{-1}$. The behavior of the inferred intensities below this wavenumber might at first be thought to result from near-coincidences of lines in the 00011-00001 and 01111-01101 bands. For example, Fig. 3 shows that the P38, 36 and 34 lines of the stronger band occur at almost the same wavenumbers ($\sim 2315, 2317$ and 2319 cm^{-1}) as three lines in the weaker band. However, Fig. 5 shows that it is only the P38 and P34 lines whose inferred intensities are greater than the extrapolated band contour. This very same behavior is observed for these three lines in the measured spectrum after its resolution has been enhanced by spectral deconvolution (see Section 3.2). Moreover, the hot band lines are conspicuously absent in the resolution-enhanced spectrum.

* NOTE: The vertical scales for the stick spectra in Figs. 4 and 5 are not the same; i.e., the lines have been normalized to maximum intensity.

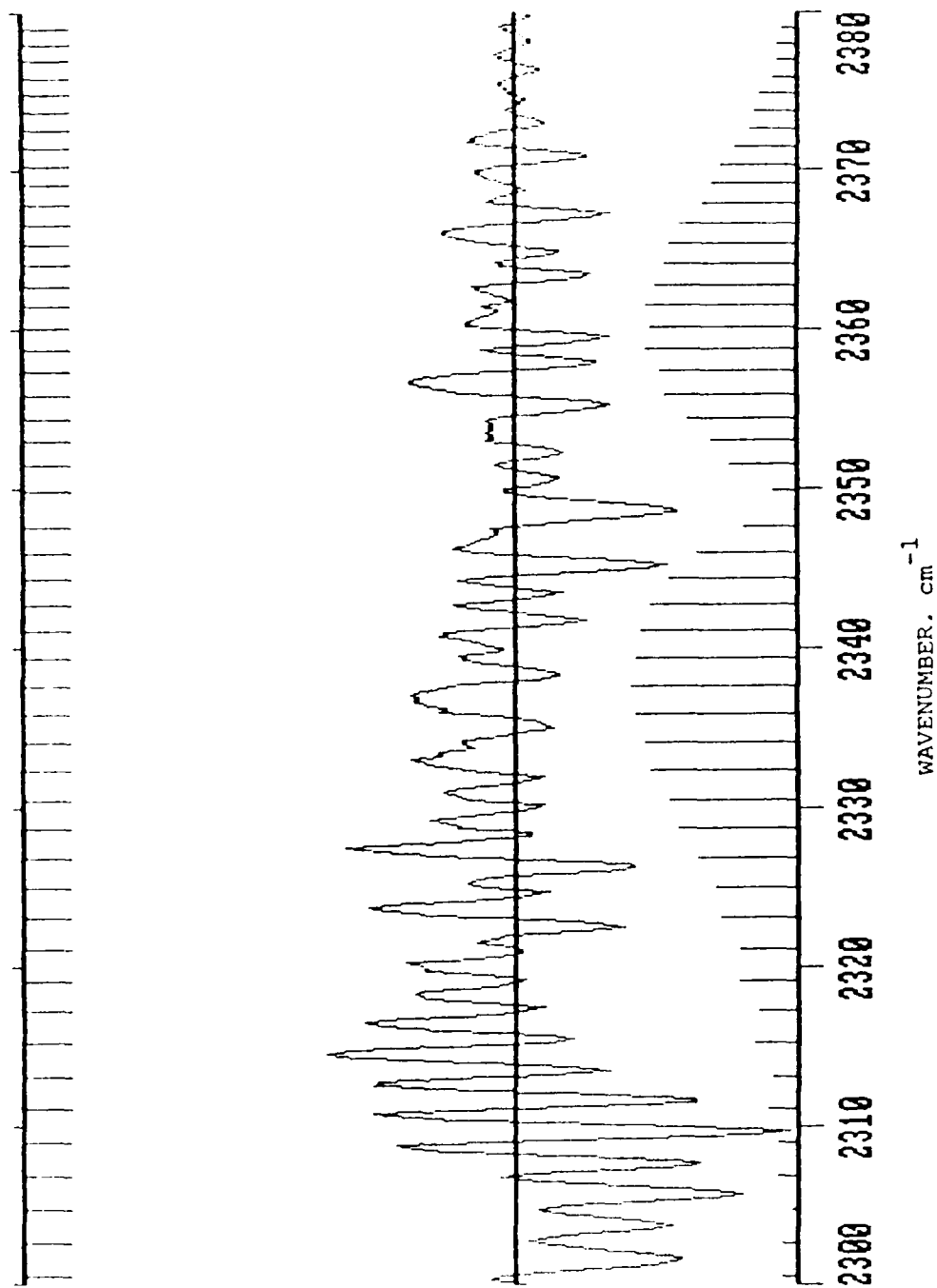


Figure 6. Upper section: Residual spectrum error.
 Lower section: Inferred line intensities. The rms of the residual error is four percent of the maximum spectral radiance.

For the reasons indicated, the irregularities in the inferred 00011-00001 intensities were attributed to overlapping NO^+ bands rather than the strongest overlapping CO_2 hot band. As will be described, we attempted to simultaneously estimate the overlapping contours of the CO_2 00011-00001 band and several NO^+ bands while ignoring possible contributions from the CO_2 01111-01101 hot band.

Table 2 lists the CO_2 line positions, their inferred intensities, and the intensities computed with the NLTE code. It should be noted that the inferred intensities are roughly 11 times smaller than the computed ones. However, the contours of the two sets are very similar (compare Figs. 4 and 5, lower sections).

In summary, the least-squares method for estimating individual line intensities has yielded excellent results for the ν_3 band of CO_2 . The rms of the residual error is only four percent, which is rather small considering that errors would be expected to arise from imprecise calibration of a nonlinear wavenumber scale (i.e., from fine-grained spectral variations in index of refraction of the field-widening/retarding wedge), from unknown effective source variations during the scan, and from instrument/detector noise. Note (Fig. 6) that if the region below $\sim 2330 \text{ cm}^{-1}$ and the region of the band origin are excluded, the maximum residual error is roughly five percent and the rms of the residual is considerably smaller than the four percent quoted above.

2.3.2 Band Contours

It is seen from Fig. 3 that the P and R branches of the $\text{C}^{12}\text{O}_2^{16}$ 00011-00001 band have peaks near $J \approx 12$ or 14. For these branches we used the basis functions given by Eqs. (11) through (12a), with $J_j = 2, 6, 10, 14, 18$ and 22. This represents a total of six basis functions for each branch or 12 for the entire CO_2 band. As a test to determine whether this was an adequate basis set we performed the following computations: We first

Table 2. CO₂ (00011-00001) Line Positions (cm⁻¹) and Intensities (W/cm² sr).

POSITION	INTENSITIES		POSITION	INTENSITIES	
	INFERRED	NLTE CODE		INFERRED	NLTE CODE
2300.4264	.1102E-10	.12648E-10	2349.9175	.1154E-10	.17892E-09
2302.6503	.10800E-10	.19299E-10	2351.4477	.3826E-10	.5321E-07
2304.8602	.25987E-11	.29195E-10	2352.9551	.50957E-10	.73358E-09
2306.9262	.11206E-10	.43656E-10	2354.4338	.69936E-10	.96281E-09
2309.0291	.10525E-10	.64329E-10	2355.8899	.83365E-10	.10817E-08
2311.1060	.17474E-10	.93209E-10	2357.3312	.86566E-10	.11498E-08
2313.1599	.17818E-10	.13245E-09	2358.7277	.95692E-10	.11757E-08
2315.1297	.30626E-10	.18424E-09	2360.1095	.9412E-10	.11662E-08
2317.1994	.2678E-10	.25045E-09	2361.4664	.97720E-10	.11266E-08
2319.1767	.3975E-10	.33196E-09	2362.7985	.91045E-10	.10620E-08
2321.1347	.30781E-10	.42963E-09	2364.1958	.84574E-10	.97711E-09
2323.0674	.50874E-10	.53850E-09	2365.3682	.81420E-10	.87710E-09
2324.9764	.53480E-10	.65790E-09	2366.6457	.74405E-10	.7672E-09
2326.8611	.65621E-10	.78158E-09	2367.8782	.60644E-10	.65764E-09
2328.7311	.7901E-10	.90725E-09	2369.0958	.54954E-10	.54178E-09
2330.5517	.84534E-10	.10165E-08	2370.2684	.48889E-10	.43693E-09
2332.3694	.96189E-10	.11122E-08	2371.4251	.38963E-10	.34268E-09
2334.1569	.98976E-10	.11870E-08	2372.5586	.30428E-10	.26179E-09
2335.9199	.10563E-09	.12351E-08	2373.6662	.25287E-10	.19480E-09
2337.6586	.10673E-09	.12518E-08	2374.7487	.22497E-10	.14160E-09
2339.3729	.10266E-09	.12322E-08	2375.8061	.14447E-10	.10964E-09
2341.0639	.97580E-10	.11720E-08	2376.8383	.11889E-10	.70104E-10
2342.7277	.89688E-10	.10650E-08	2377.8455	.12667E-10	.47978E-10
2344.3685	.79233E-10	.99287E-09	2378.8274	.70503E-11	.3231E-10
2345.9047	.59970E-10	.67738E-09	2379.7942	.56880E-11	.2157E-10
2347.5763	.32938E-10	.37864E-09	2380.7159	.50574E-11	.14209E-10

convolved the stick spectrum representing the computed (NLTE) 00011-00001 line intensities with the shift-variant FWI apparatus function L_{ij} , defined by Eqs. (14) through (16). This theoretical spectrum was then analyzed as data; i.e., we solved for the vector c' of weights for the above-described basis functions. Using the solution c' we then reconstructed the spectrum, and computed the rms difference between it and the original theoretical spectrum. This rms difference was only 0.2 percent of the maximum theoretical spectral radiance. Various other selections for the J_j 's resulted in larger rms differences.

The spectral region $2300\text{--}2380\text{ cm}^{-1}$ also includes portions of the following branches of NO^+ bands:

- 1-0: P and R
- 2-1: P and R
- 3-2: R
- 4-3: R

One basis function was used for each of these six branches. Each had an α_j corresponding to the value $J_j \equiv J_1 = 6$, based on computations performed by J. Winick of AFGL. The analysis included the contributions of lines located within "guardbands" of width 20 cm^{-1} above and below the $2300\text{--}2380\text{ cm}^{-1}$ region of interest. The NO^+ line positions required in the analysis were supplied by J. Winnick.

The method described in Section 2.1.2 was used to estimate the scan 10 CO_2 band contour (two branch contours) and the four NO^+ band contours (six branch contours listed above). That is, we solved for the partitioned vector c' given by Eq. (10), which determines these contours and the corresponding CO_2 and NO^+ line intensities. Figure 7 shows the inferred line intensities plotted as stick spectra. The upper part shows only the CO_2 intensities; the lower part shows both the CO_2 and NO^+ intensities.

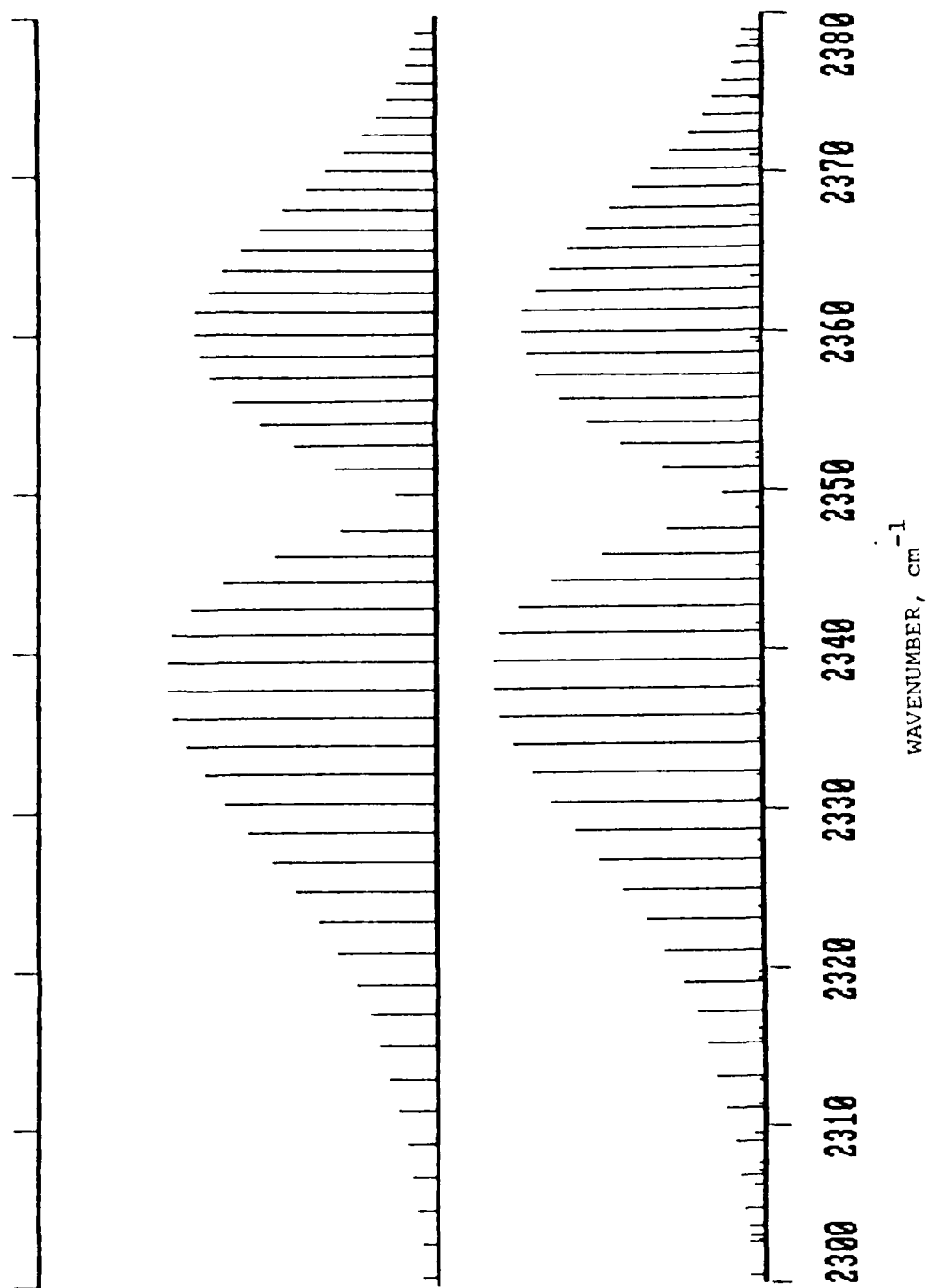


Figure 7. Upper section: CO₂ line intensities obtained from inferred band contour.
 Lower section: Same, except inferred NO⁺ line intensities are also shown.

Table 3 lists the inferred CO_2 line intensities. The apodization parameter c is unity for these results.

A comparison of Tables 2 and 3 show that the inferred CO_2 intensities have not changed by very much, but, of course, the new estimates follow a very smooth contour. Figure 7 shows that the inferred NO^+ intensities are very low in comparison to those for CO_2 . The maximum inferred line intensity for each NO^+ band relative to the maximum inferred CO_2 line intensity is

- 1-0: ~3.6 percent
- 2-1: ~5.0 percent
(~2.5 percent for R-branch only)
- 3-2: ~1.0 percent
- 4-3: ~6.0 percent (occurs near 2303 cm^{-1})

The values of five and six percent for the 2-1 and 4-3 bands, respectively, represent lines near 2300 cm^{-1} where the residual spectrum error is high (~10 percent of the maximum observed spectral radiance). The inferred intensities for the NO^+ 1-0 and 2-1 bands are plotted on normalized scales in Fig. 8.

The residual spectrum is not shown, but it bears a strong resemblance to the one in Fig. 6. The maximum and rms residuals relative to the maximum observed spectral radiance are 10 and 3.8 percent, respectively, compared to 13 and ~4 percent for the method represented by Fig. 6. In other words, inclusion of NO^+ has not effected a significant reduction in the residual. Based on these facts and the very small ratio of inferred NO^+ intensities to CO_2 intensities, it is felt that the present results are inconclusive in establishing that NO^+ was observed by the FWI.

Table 3. CO₂ Line Intensities Inferred by Band Contours Least-Squares Method.

POSITION (cm ⁻¹)	INTENSITY (W/cm ² sr)	POSITION (cm ⁻¹)	INTENSITY (W/cm ² sr)
2300.4764	.55375E-11	2349.9176	.16131E-10
2302.6507	.68361E-11	2351.4477	.42144E-10
2304.8002	.93647E-11	2352.9531	.59097E-10
2305.9262	.10246E-10	2354.4332	.72944E-10
2309.9281	.12567E-10	2355.8999	.96517E-10
2311.1060	.15441E-10	2357.3212	.95305E-10
2313.1599	.18980E-10	2358.7277	.10041E-09
2315.1897	.23313E-10	2360.1095	.10204E-09
2317.1954	.29556E-10	2361.4664	.10058E-09
2319.1769	.34802E-10	2362.7985	.96435E-10
2321.1343	.42093E-10	2364.1058	.90072E-10
2323.0674	.50392E-10	2365.3887	.82074E-10
2324.9764	.59558E-10	2366.6457	.73070E-10
2326.9611	.69324E-10	2367.8782	.63665E-10
2328.7215	.79291E-10	2369.0858	.54389E-10
2330.5577	.89949E-10	2370.2684	.45649E-10
2332.3694	.97729E-10	2371.4261	.37731E-10
2334.1569	.10509E-09	2372.5536	.30760E-10
2335.9199	.11059E-09	2373.6661	.24312E-10
2337.6586	.11384E-09	2374.7487	.19647E-10
2339.3728	.11441E-09	2375.9061	.15792E-10
2341.0625	.11146E-09	2376.8383	.12907E-10
2342.7277	.10357E-09	2377.8455	.98984E-11
2344.3685	.89198E-10	2378.8274	.78199E-11
2345.9847	.67893E-10	2379.7842	.61997E-11
2347.5763	.39113E-10	2380.7158	.49061E-11

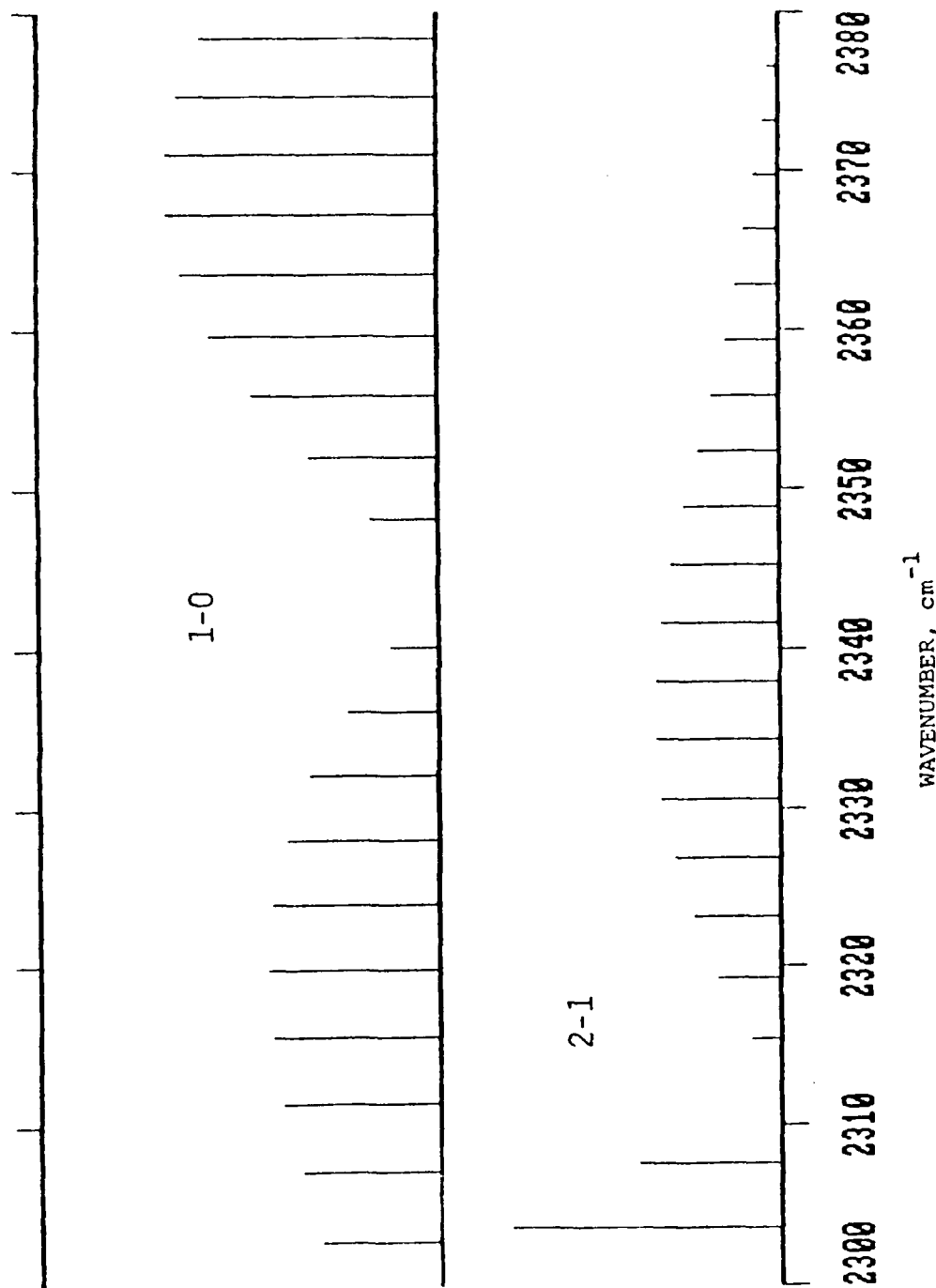


Figure 8. Inferred line intensities for the NO⁺ 1-0 and 2-1 bands.
See text for a discussion of the significance of these results.

2.4 Application to the 2220-2300 cm⁻¹ Region

The spectral region 2220-2300 cm⁻¹ is probably optimum for the detection of NO⁺ in the FWI spectra. This portion of the spectrum for scan 10, unapodized, was analyzed by the method of Section 2.1.2, which estimates overlapping band contours. The analysis assumed that the measured emissions are due to the following NO⁺ bands/branches:

- 1-0: P
- 2-1: P
- 3-2: P and R
- 4-3: P and R
- 5-4: R
- 6-5: R

Again, one basis function was used for each of these eight NO⁺ branches. The parameter $J_j \equiv J_1$, which determines the location of the basis function peaks, was varied between 6 and 10. Only lines with predicted intensities greater than approximately two percent of the maximum predicted line intensity in each branch were included; J. Winick provided the intensity predictions. The total number was 111 lines of NO⁺. The contributions from CO₂ lines near 2300 cm⁻¹ or higher wavenumbers were assumed to be negligible.

The measured spectral radiance in the 2220-2300 cm⁻¹ region increases significantly between scans 9 and 10 and between scans 10 and 11; i.e., it was apparently increasing during scan 10. Since the optical retardation decreased with time during the scan, it is appropriate to select a value less than unity for the source-change parameter c . This parameter was varied from 0.005 through unity to 1.4.

Figure 9 shows the USU measured spectrum and typical spectra reconstructed from the least-squares inferences. The agreement between the measured and reconstructed spectra is obviously very poor. For $c = 0.3$

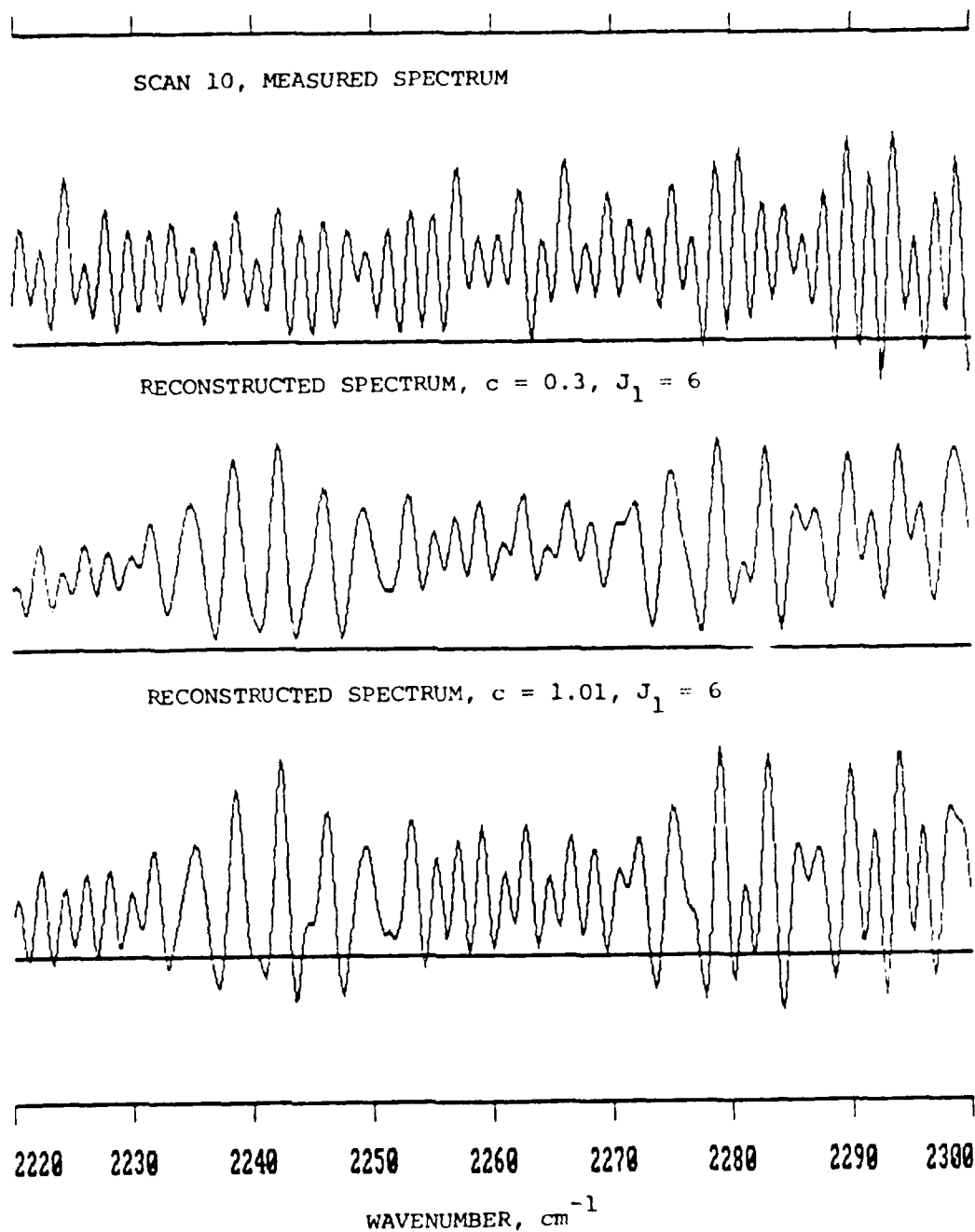


Figure 9. Measured spectrum for scan 10 and two spectra reconstructed from inferred NO^+ band contours and line positions.

the rms difference is approximately 22 percent and the maximum difference is approximately 67 percent; for $c = 1.0$ these differences are 27 percent and 86 percent. The smallest rms difference obtained for the entire range of variation of c and J_j was approximately 21 percent. Similarly, the maximum difference could not be reduced below approximately 57 percent. These results indicate that the measured spectrum is not due to NO^+ .

SECTION 3

DECONVOLUTION ANALYSIS OF FWI SPECTRA

3.1 Background

The least-squares methods described above rely on knowledge of the particular radiators present in the source and on the positions of their spectral lines. If this information is lacking, or if errors in the calibrated wavelength scale are suspected, these methods are not applicable or marginally useful. The present section describes and applies a technique for recovering "superresolved" spectra in Fourier transform spectroscopy, i.e., of obtaining spectral resolution higher than that provided by conventional FFT analysis of interferograms. If the achieved resolution is high enough, the spectra may reveal sequences of lines (or band contours) that are recognized as belonging to a particular species; resolved (isolated) lines can be integrated to obtain their intensities. With these possibilities in mind we coded the technique and applied it to the 2220-2300 cm^{-1} and 2300-2380 cm^{-1} regions of several FWI spectra. In particular, we wanted to find out which species, if not NO^+ , is (are) responsible for the observed emissions between 2220 and 2300 cm^{-1} .

Modern methods of signal recovery and spectral estimation include the Maximum Entropy Method (MEM), the related Linear Prediction (LP) and Autoregressive (AR) techniques, Maximum Likelihood (ML), Minimum Cross Entropy (MCE), and constrained nonlinear deconvolution. They are often used with the objective of removing, to the extent possible, the blurring effect of the measuring instrument, i.e., to recover fine structure in a measured or inferred spectrum or spatial detail in an image. For this type of application they may all be characterized as constrained (linear or nonlinear) methods of deconvolution, even though some operate on transforms of the desired signal. The methods referred to have been demonstrated to achieve resolutions substantially greater than the limits implicit in the

"Blackman-Tukey" approach based on Fourier analysis. These limits are defined by, for example, the width of an entrance slit, length of an interferogram, or the size of a collecting aperture or detector. A comprehensive summary of the methods available for deconvolution is given by Jansson (1984).

We first attempted to recover superresolved FWI spectra in the region of the ν_3 CO_2 band ($2300\text{--}2380\text{ cm}^{-1}$) by the MEM. The result, shown in Fig. 10, exhibits superresolution, but the CO_2 line positions are not accurately reproduced. Specifically, the line spacing in the R-branch is just slightly less than that in the P-branch; the ratio at the branch maxima ought to be $\sim 1.35/1.8 = 0.75$. Also, the gap at the band origin is too large. The wavenumber scale in Fig. 10 is not calibrated. However, calibration would not produce a significant change in the ratio of line spacings for the two branches.

There are many examples in the literature of the successful use of the MEM to obtain superresolution (with correctly reproduced line positions) in the case of spectra with ~ 10 or fewer lines that are not uniformly spaced. There have not been, at least to our knowledge, any similarly successful demonstrations for spectra containing a large number of lines (say, 80 or more) with pseudo-regular spacing like the CO_2 ν_3 band.

After this experience with the MEM we selected the Jansson method of constrained nonlinear deconvolution for use in analyzing FWI spectra; see Jansson (1984). The latter has been proven to work well for arbitrarily complicated spectra, although its superresolution capability is not nearly as dramatic as that of the MEM applied to simple spectra.

3.2 Jansson's Method

Jansson's method of constrained nonlinear deconvolution is an outgrowth of the linear deconvolution method of Van Cittert. The nonlinearity of the Jansson algorithm is the result of a constraint that suppresses

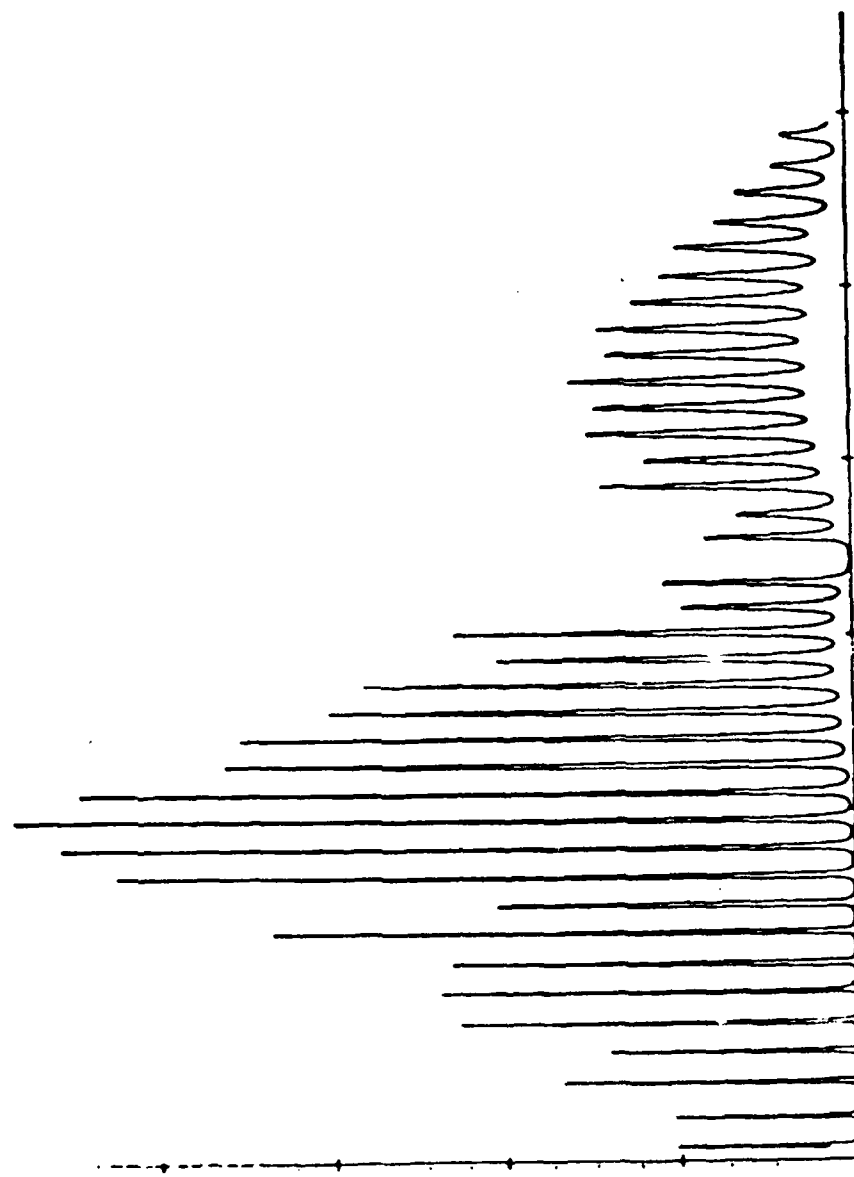


Figure 10. Maximum entropy spectrum computed for scan 10.

unphysical negative sideloads that tend to be generated by the Van Cittert algorithm (even when the apparatus function is positive definite); see Jansson (1984), pp. 71-73. This constraint results in a greatly improved capability to enhance spectral resolution.

The following notations will be used in describing the Jansson algorithm:

- O_i = the sought-after "object" spectrum, i.e., the true source spectrum,
- I_i = the "image" or observed (degraded) spectrum, formerly denoted $S(v_i)$,
- L_{ij} (or L_{i-j}) = the shift-variant (or invariant) apparatus function,
- $()^k$ = superscript denoting the iteration cycle.

The algorithm is

$$O_i^{(k+1)} = O_i^{(k)} + R(O_i^{(k)}) \left\{ I_i - (L * O^{(k)})_i \right\} \quad (18)$$

where $*$ denotes convolution, and R is a "relaxation function" to be defined subsequently. The superscripts on the O_i involved in the convolution are not defined, to indicate that the "point-successive" method of evaluation is used. That is, values of O_i that have already been calculated in the current $(k+1)$ st cycle are used; the remaining values of O_i represent the previous (k) th cycle. Thus, the convolution term is

$$(L * O^{(k)})_i \equiv \sum_{j < i} L_{ij} O_j^{(k+1)} + \sum_{j \geq i} L_{ij} O_j^{(k)} . \quad (19)$$

This expression belies the simplicity of the algorithm. Note that the O_i can be stored in a single array; any element $O_i^{(k)}$ is recomputed as

$O_i^{(k+1)}$ by Eq. (18). The convolution in Eq. (18) uses the current array, i.e., the array elements corresponding to the current values of i and k . This method of evaluation has been found to be more rapidly convergent than the "point-simultaneous" method, which uses the convolution of L and $O^{(k)}$, and hence requires the storage of both $O^{(k)}$ and $O^{(k+1)}$.

Equation (18) is the Van Cittert algorithm if the relaxation function R is set to unity. In this case the difference between the current and previous estimates of the object spectrum is equal to the difference between the image spectrum I and the current "reconstructed image" spectrum $L * O^{(k)}$. This difference is zero if $O^{(k)} = I$ or when the process has converged.

Generally, the initial guess $O^{(0)}$ is taken as I . Suppose the true spectrum (object) is a single isolated line. Then $L * O^{(0)}$ will be broader than I , and the bracketed term in Eq. (18) will be positive near the line center and negative in the line wings (assuming the apparatus function L is normalized, positive definite and monotonically decreasing away from the line center, like a Gaussian). Consequently, $O^{(1)}$, evaluated by the Van Cittert algorithm, will be bigger than $O^{(0)}$ at the line center, and will have negative "sidelobes". To suppress this undesirable effect, Jansson chose a relaxation function $R(O_i^{(k)})$ that is negative when $O_i^{(k)}$ is negative. In fact, Jansson used the relaxation function pictured in the upper part of Fig. 11, which is negative when $O_i^{(k)}$ is negative or greater than unity. Jansson was interested in deconvolving absorption spectra; i.e., values outside the range $0 \leq O_i^{(k)} \leq 1$ are unphysical. This relaxation function is given by

$$R(O_i^{(k)}) = \frac{P_0}{L_{ii}} \left(1 - 2|O_i^{(k)} - 1/2| \right), \quad (20)$$

where P_0 is an adjustable parameter that controls the "strength" of the relaxation function.

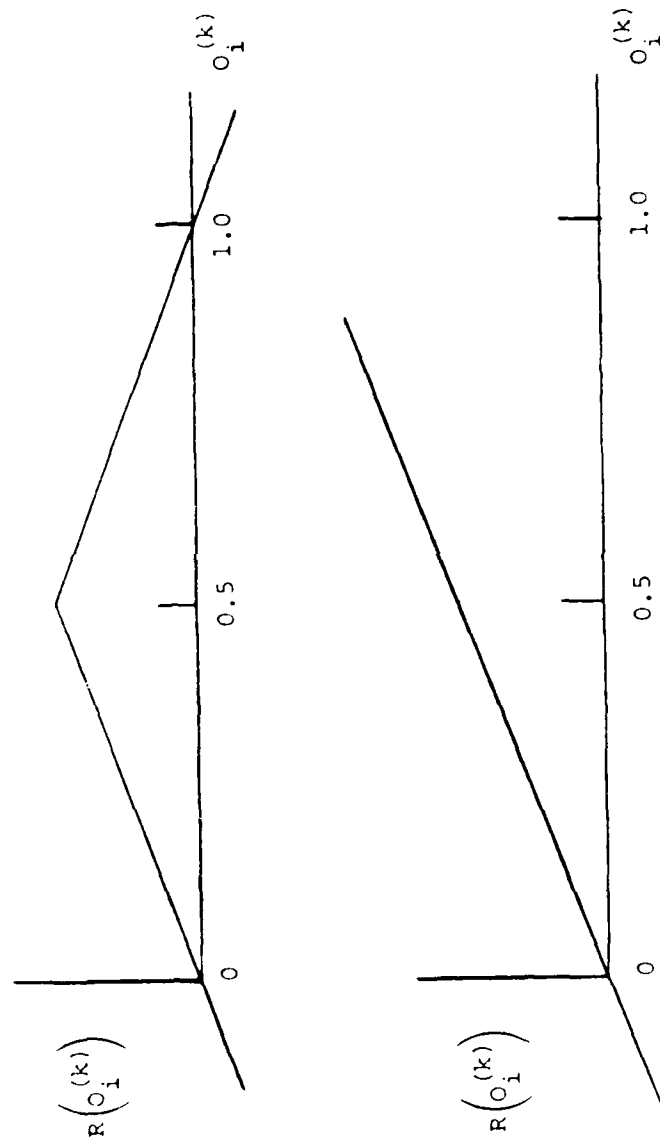


Figure 11. Upper section: Relaxation function used by Jansson (1984) for deconvolving absorption spectra.
Lower section: Relaxation function used in the present study.

Since the present study is concerned with emission spectra, we used the monotonically increasing relaxation formula

$$R(O_i^{(k)}) = \frac{R_0}{L_{ii}} 2 O_i^{(k)} / \max[O_i^{(k-1)}] \quad (21)$$

which is pictured in the lower part of Fig. 11. Equations (20) and (21) give approximately the same value when $O_i^{(k)}$ is less than one-half its maximum value. In our application, O and I have units of spectral radiance.

The Jansson method with the minimum negativity constraint imposed by the relaxation function (20) or (21), presupposes a positive definite apparatus function. This can be achieved in Fourier transform spectroscopy by appropriate apodization of the interferogram. The apodization will result in an immediate loss in spectral resolution (equivalent to a factor of two or more), but will also reduce the amplitude of, or even eliminate, the sidelobes of the apparatus function. We elected to use triangular apodization. It will be demonstrated that the Jansson algorithm can recover much more than the factor-of-two initial loss in resolution and virtually eliminate the residual "artifacts", i.e., the sidelobes of the new sinc-squared apparatus function.

We did not actually apply triangular apodization to the FWI interferograms, but rather convolved the FWI spectra with the corresponding shift-variant apparatus function. This apparatus function is obtained by substituting $[(\sin q/2)/(q/2)]^2/(2\Delta\sigma)$ for $L(\sigma_i, \sigma_j)$ in Eq. (14); i.e., this sinc-squared function replaces the sinc function $(\sin q/q)/\Delta\sigma$ given by Eq. (16). By performing spectral convolution rather than interferogram apodization, we avoided having to repeat the calibrations (both wavelength scale and spectral responsivity) and interpolation performed by USU.

Recall that in the least-squares analysis of FWI spectra we allowed for an exponential source variation characterized by the parameter c (Section 2.2). To represent the same effect in the present deconvolution analysis, the apparatus function L must be modified to include the source exponential self-apodization: L is given by Eq. (14) with

$$L(\sigma_i, \sigma_j) = \frac{1}{\Delta\sigma} \frac{1}{D} \left\{ c \left(\ln c + \frac{N}{D} \right) \cos q + \frac{2c(\ln c)q}{D} \sin q - (\ln c)(1+c) - \frac{N}{D} \right\} \quad (22)$$

where

$$\begin{aligned} N &\equiv (\ln c)^2 - q^2 \\ D &\equiv (\ln c)^2 + q^2 \end{aligned} \quad (23)$$

and where $q = \pi[\sigma(v_i) - \sigma(v_j)]/\Delta\sigma$, as before. This apparatus function $L(\sigma_i, \sigma_j) \equiv L(q)$ is the Fourier transform of an exponential $\exp(-|ax|)$ times a triangle. It reduces to the $\text{sinc}^2(q/2)$ function described above when $c = 1$.

Note that two different apparatus functions are involved in the deconvolution analysis. The first is convolved with the USU-computed spectrum to produce the effect of triangular apodization. Any effects of a varying source are already present in this image spectrum. The second apparatus function, defined by Eqs. (14), (22) and (23), is used in the deconvolution algorithm, Eq. (18). It accounts for the triangular apodization and the possibility of a varying source ($c \neq 1$).

Jansson points out the importance of smoothing the original data and also of smoothing the result of each iteration cycle to prevent the buildup of high-frequency noise; see Jansson (1984) and works cited on pg. 106 of this reference. Pliva, et al (1980) emphasize the smoothing

requirement as well as the need for high signal-to-noise in the original data spectrum. We used essentially the same smoothing procedures as Jansson. Like Jansson, we used a smoothed version of the data spectrum as the initial guess for the object spectrum.

The FWI spectra provided by USU consist of points spaced 0.25 cm^{-1} apart. As mentioned above, the spectral resolution is approximately 1 cm^{-1} unapodized, or $\sim 2 \text{ cm}^{-1}$ apodized. The 0.25 cm^{-1} spacing is not adequate if convolutions are performed by the simple rectangular integration implied by Eq. (19). We therefore interpolated the data to obtain eight times as many points. The interpolation was performed as part of the initial convolution that effected triangular apodization; i.e., the convolution lags were multiples of $0.25/8 \text{ cm}^{-1}$.

The computer code written to perform the Jansson deconvolution was applied, during the final debugging phase, to the case in which the image spectrum is due to a source consisting of just a few delta-function emission lines. The artificial image spectrum, after the initial convolution/interpolation step, consisted of sinc-squared lines whose widths correspond to spectral resolution $\Delta\nu \approx 2 \text{ cm}^{-1}$. One such spectrum is shown in the top panel of Fig. 12. It has two lines separated by 2.5 cm^{-1} and a third, isolated line. The middle and bottom panels show the deconvolved spectrum after ten and 20 iterations, respectively. For all deconvolutions performed in this study the relaxation strength parameter R_0 was fixed at 0.1 for the first half of the iterations and at 0.2 for the second half.

Note that the resolution (based on FWHM) is enhanced by roughly a factor of three in this noise-free case, and that the sidelobes have all but disappeared after 20 iterations. Most of the increased resolution is gained in the first 10 cycles, but the relative sidelobe amplitude continues to decrease between the 10th and the 20th cycle. It should be noted that the maximum in each spectrum is plotted to the same height; a plot in absolute units would demonstrate that the line intensities are preserved.

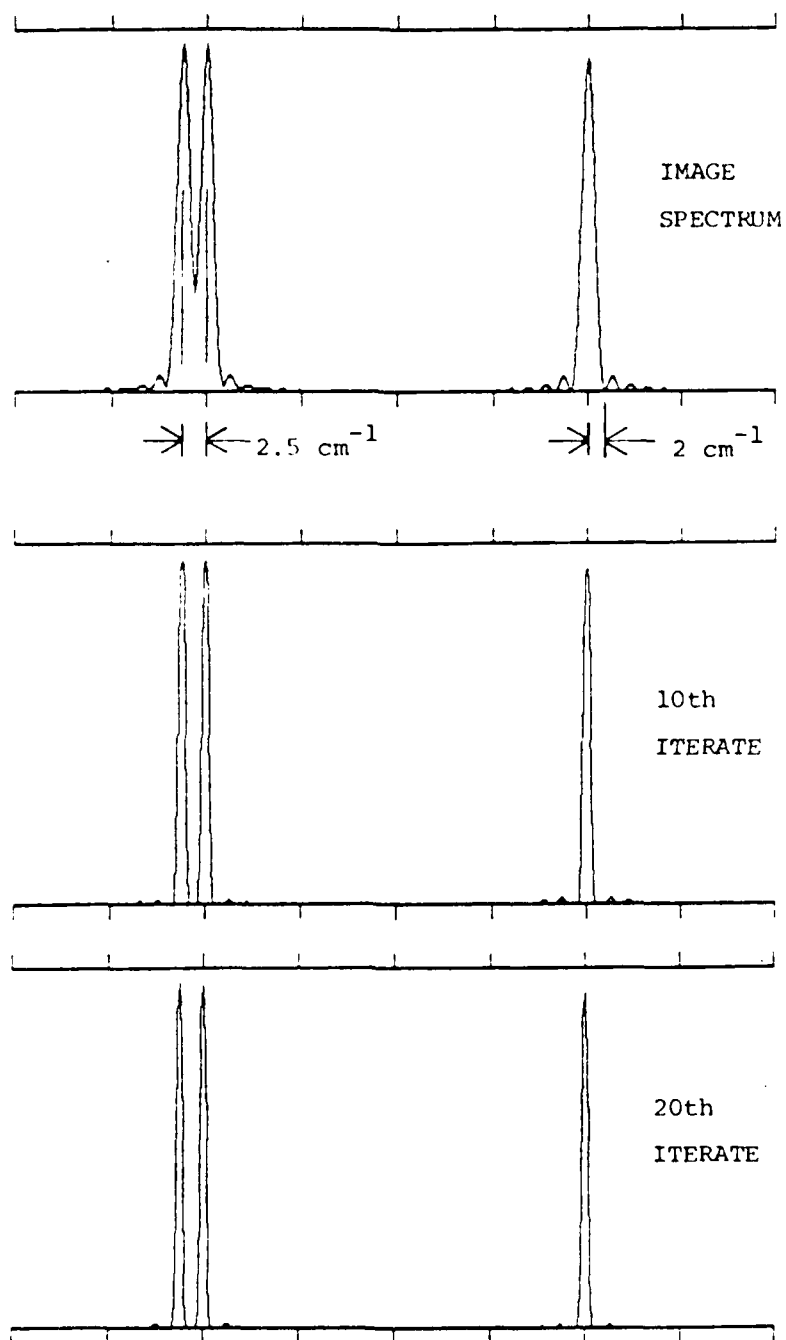


Figure 12. Image spectrum of sinc-squared lines, and deconvolved spectra after 10 and 20 iterations.

Figure 13 shows the initial spectrum and deconvolved result after 20 iterations when the two closely spaced lines are 1.25 cm^{-1} apart, i.e., are unresolved in the image spectrum. The algorithm succeeds in resolving the two lines, but does not eliminate their overlap entirely, despite the fact that the final base width of the isolated line is approximately 1.25 cm^{-1} .

3.3 Application to the $\nu_3 \text{ CO}_2$ Band

The Jansson method was used to deconvolve the spectral region $2290\text{--}2390 \text{ cm}^{-1}$ of FWI scans 10 and 6. The objectives of this effort were

- a.) to further validate the method and computer code, based on the known positions of the $\nu_3 \text{ CO}_2$ lines.
- b.) to test the scan-to-scan reproducibility of the FWI spectra with respect to line positions, and
- c.) to determine if NO^+ lines of the 1-0 and 2-1 bands are present between the $\text{CO}_2 \nu_3$ lines

The spectrum computed by USU for scan 10 from a 64K unapodized interferogram was already shown in Fig. 4. Convolution of this spectrum with the sinc-squared function that effects triangular apodization yields the spectrum shown in Fig. 14. This is the starting point (image spectrum) for the deconvolution algorithm. It represents very nearly the same spectral resolution that results from Hamming apodization of a 64K interferogram. Note that very little spectral structure remains in the R-branch of the CO_2 band, where the average line spacing is approximately 1.35 cm^{-1} .

Figure 15 shows the deconvolved spectrum after 60 iterations. For this result the source apodization parameter is 1.05, representing an assumed five-percent decrease in the CO_2 column thickness during scan 10 (a "reverse" scan). Various other values up to 1.4 were tried, but these

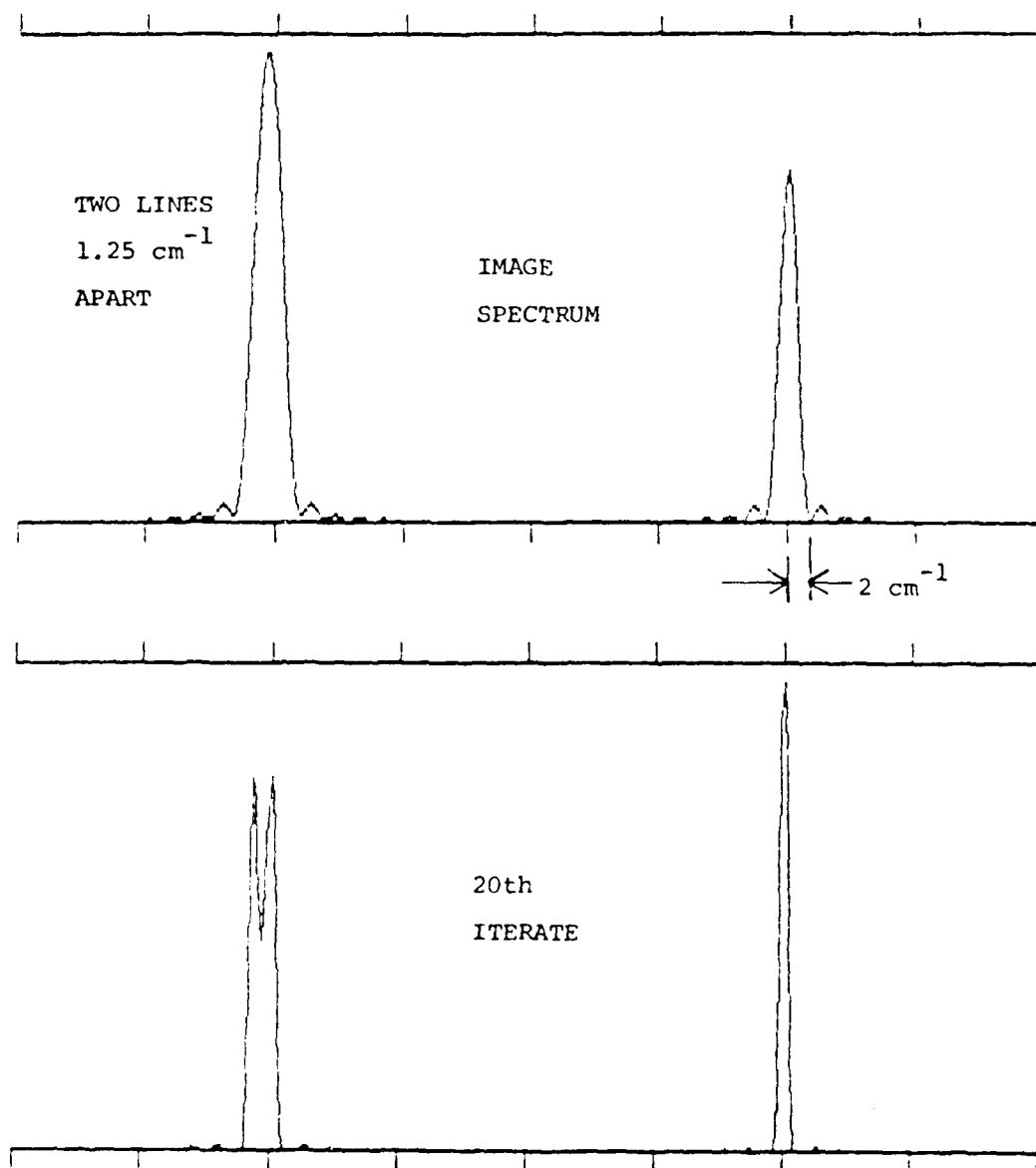


Figure 13. Same as top and bottom panels of Fig. 12, except that the two closely spaced lines are 1.25 cm⁻¹ apart (are unresolved) in the image spectrum.

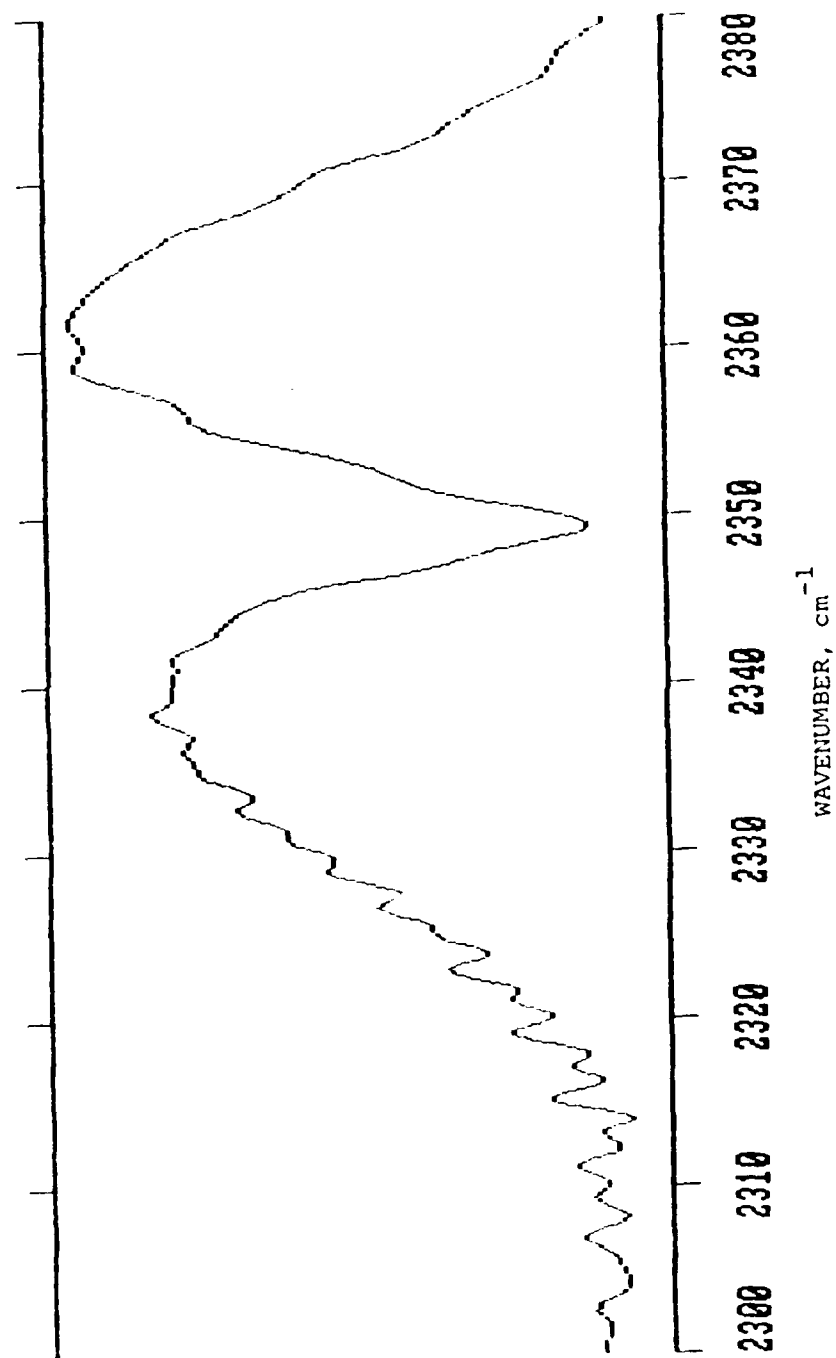


Figure 14. Measured spectrum for scan 10 convolved with a sinc-squared function to effect triangular apodization.

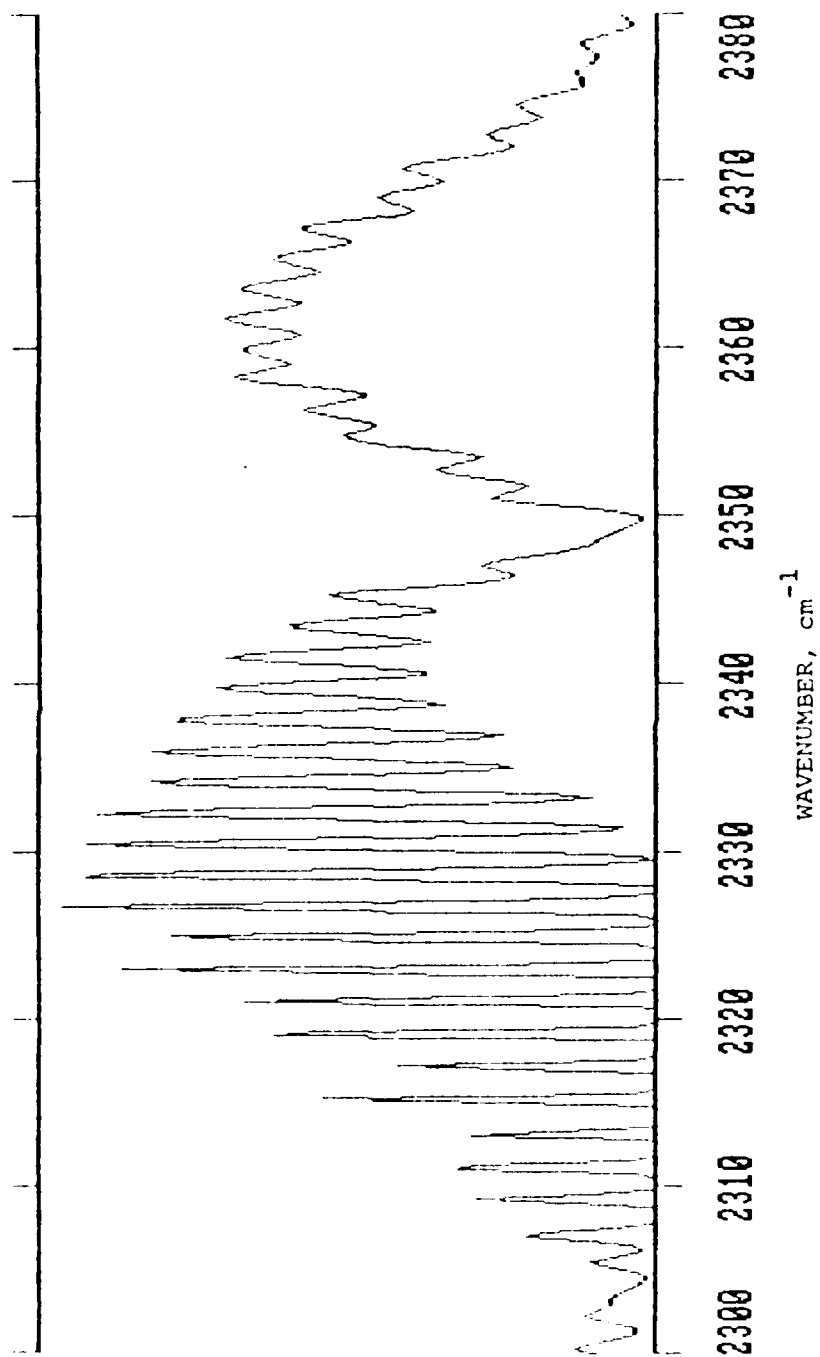


Figure 15. The result of deconvolving the spectrum of Fig. 14; 60 iterations were used with $c = 1.05$.

resulted in less resolution enhancement. Note that the resolution enhancement is very good in the red wing of the P-branch where the line spacing is approximately 2 cm^{-1} . The enhancement is relatively poor at wavenumbers larger than $\sim 2335 \text{ cm}^{-1}$.

The same deconvolved scan 10 spectrum is shown on an expanded wavenumber scale in Fig. 16, which consists of five panels covering the spectral region $2290\text{--}2390 \text{ cm}^{-1}$. Figure 17 shows the corresponding deconvolved spectrum for scan 6. Note that the plots are normalized; the maximum spectral radiance for scan 6 is roughly twice that of scan 10. A noticeable feature of the result for scan 6 is the saturated spectral radiances for many of the P branch lines, indicating that the source is optically thick in these lines. The FWI data for scan 6 was obtained at $\sim 95 \text{ km}$ altitude, whereas scan 10 data represents $\sim 101 \text{ km}$ altitude.

Figure 18 reproduces the $2310\text{--}2330 \text{ cm}^{-1}$ region of the deconvolved spectrum for scan 10. Several features are noteworthy: The positions of the CO_2 lines, especially P42 through P32, are in excellent agreement with the positions given in the AFGL line parameters compilation, which are indicated by the hash marks. Secondly, there are no lines other than the expected $\text{CO}_2(v_3; 00011\text{--}00001)$ lines. In particular, lines of the 1-0 and 2-1 bands of NO^+ , which overlap the CO_2 band, are absent.* Note also that the CO_2 P42 through P28 lines seem alternately too strong or too weak. The same alternating intensity distribution was observed in the results of the least-squares analysis of scan 10 (see Section 2.3.1 and Fig. 5). Therefore it is not an artificial effect of the Jansson method. Finally, the FWHM of the deconvolved lines is ~ 0.4 to 0.5 cm^{-1} compared to $\sim 2.2 \text{ cm}^{-1}$ in the image spectrum. This represents a resolution enhancement factor of 4.4 (or ~ 2.2 if the final resolution is compared to the basic 1.1 cm^{-1} capability of the FWI).

* These NO^+ lines have the positions shown in Fig. 8.

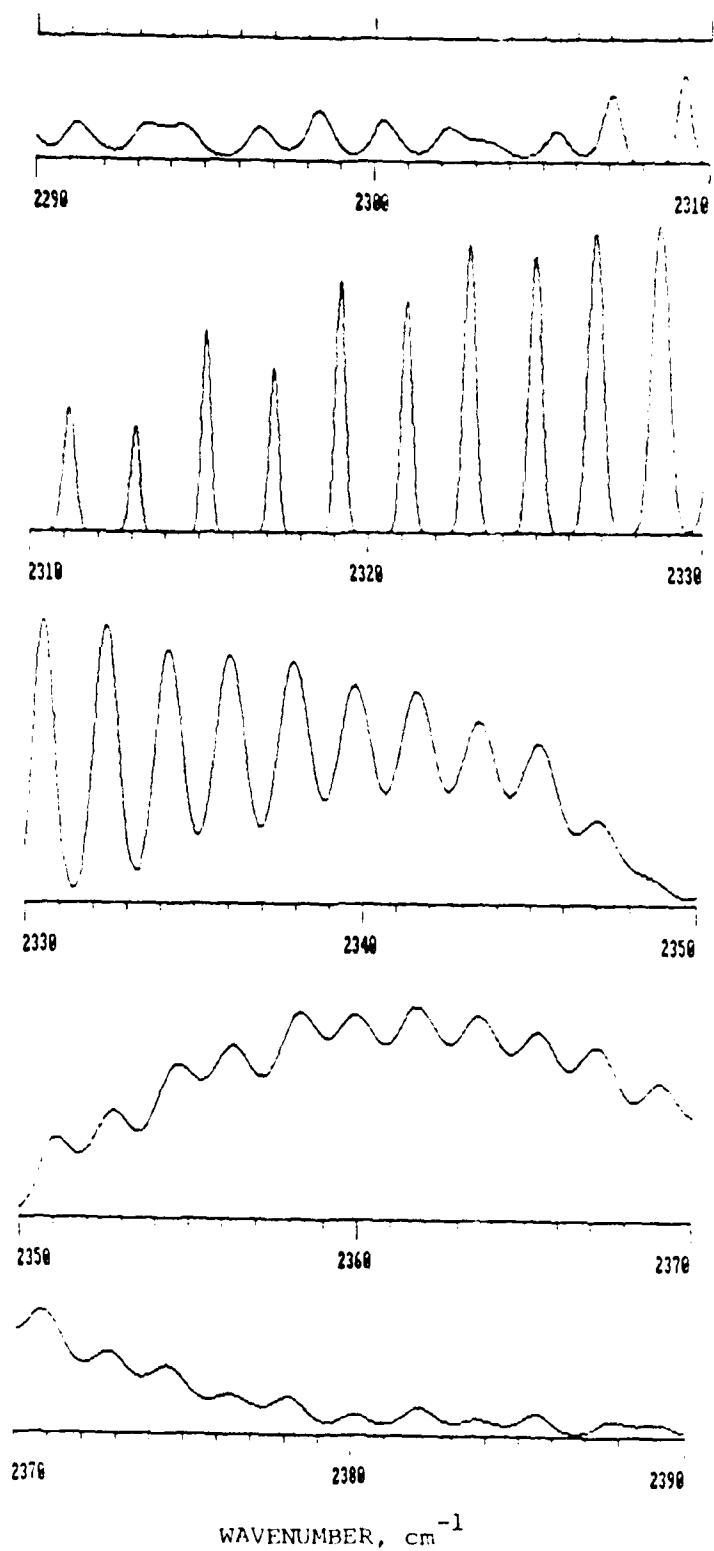


Figure 16. Same as Fig. 15, except the wavenumber scale is expanded (SCAN 10).

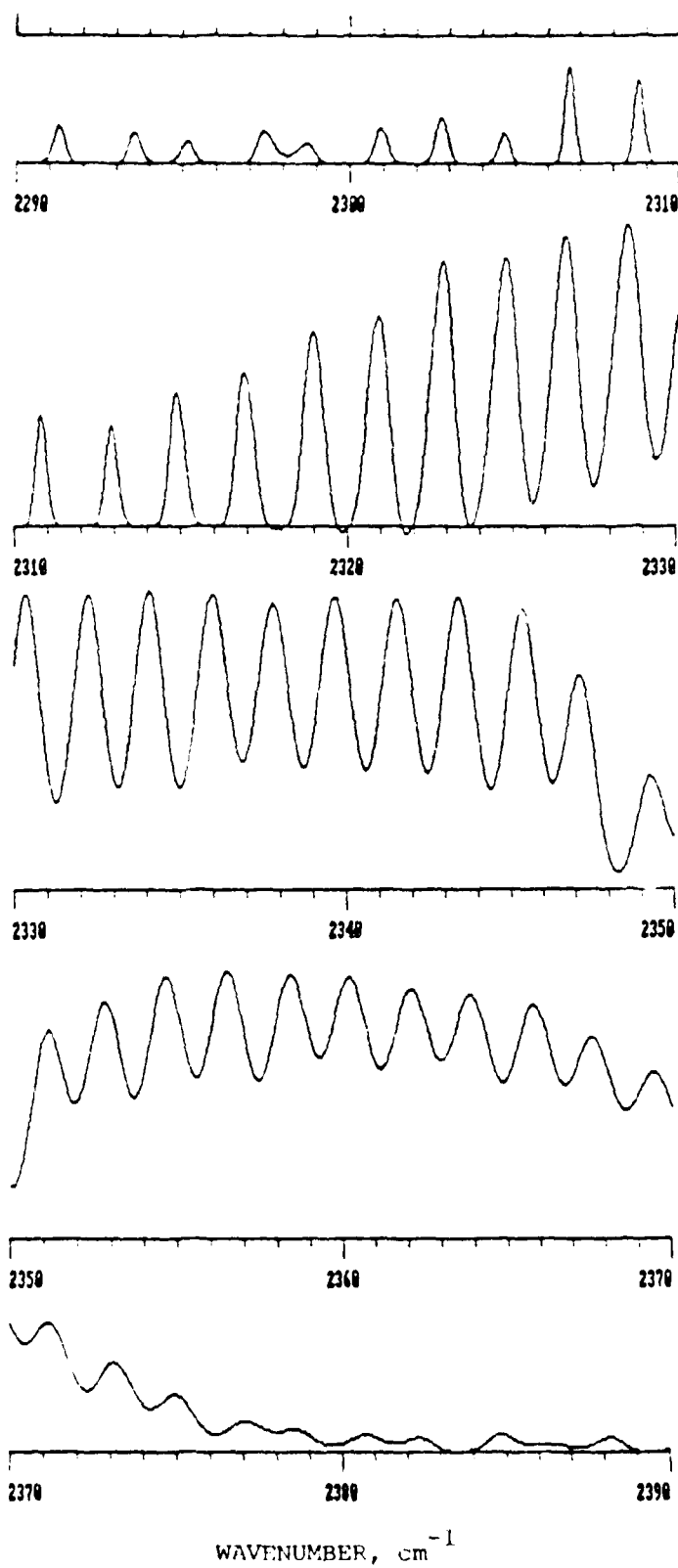


Figure 17. Same as Fig. 16, except for scan 6.

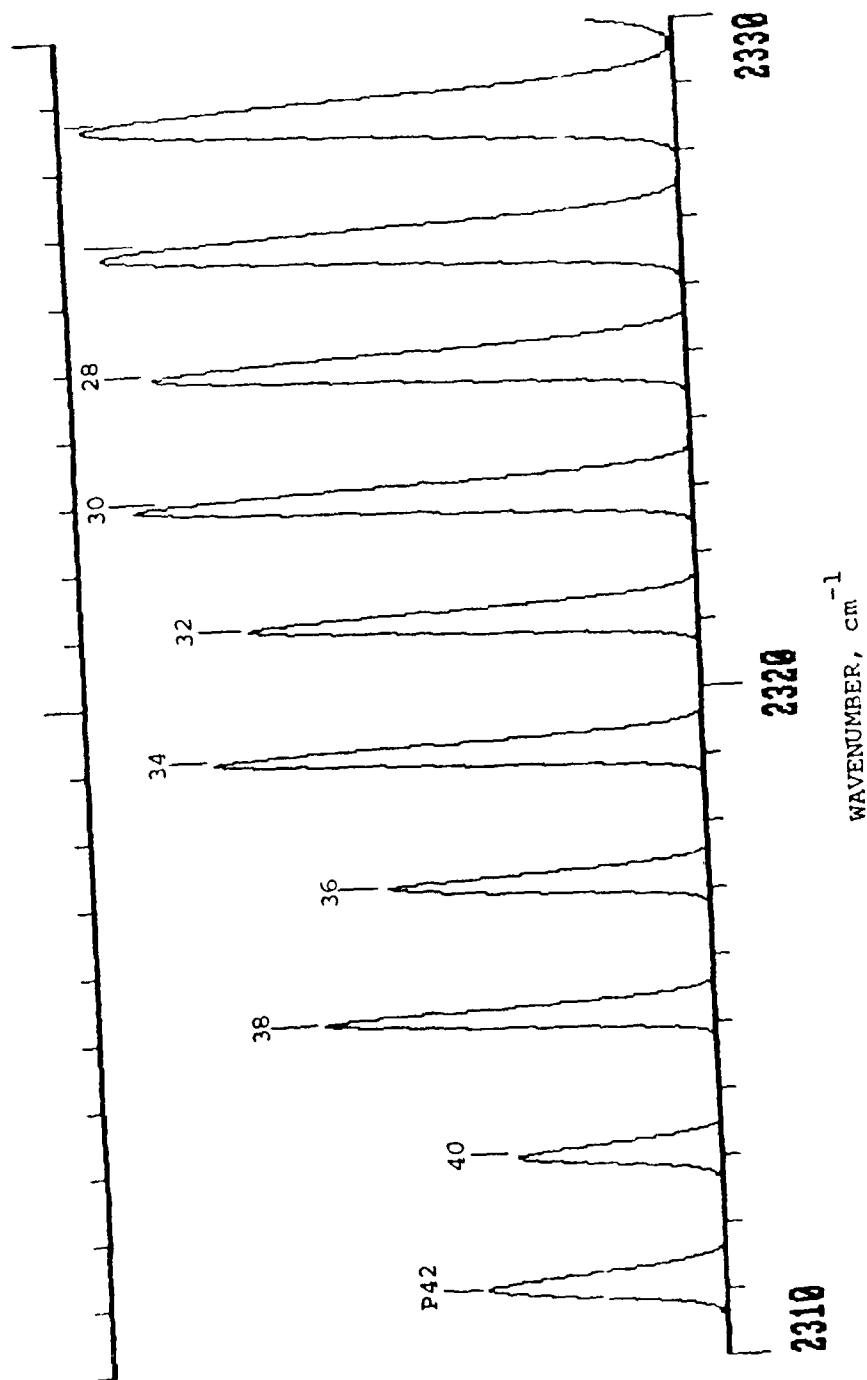


Figure 18. The 2390-2330 cm⁻¹ region of the deconvolved spectrum for scan 10. The positions of the lines agree very well with the known positions of the CO₂ P24 through P42 lines, which are indicated by hash marks. NO⁺ lines are not present.

The 2310-2330 cm^{-1} segments of the deconvolved spectra for scans 10 and 6 are compared in Fig. 19. It would appear that the wavenumber scale of scan 6 is slightly shifted and stretched relative to the scale for scan 10. Also, the resolution enhancement for scan 6 is noticeably less after the first few lines (P42 through P38). This difference in achieved resolution is possibly related to the existence of both thin and thick lines in the spectrum: the part of the apparatus function due to source variations may be quite different for the thin and thick regions. We used $c = 1.05$ and 60 iteration cycles in deconvolving scan 6; c was not varied. Perhaps this value of c was not appropriate for scan 6 (or for the self-absorbed lines of scan 6).

Unexplained shifts are also present in spectra computed by USU from 64K, Hamming-apodized interferograms. Four such spectra representing four consecutive scans are shown in Fig. 20. Spectrum 11 appears to be shifted relative to spectrum 10.

3.4 Application to the 2220-2300 cm^{-1} Region

FWI data for this spectral region were deconvolved in the same manner as for the 2300-2380 cm^{-1} region, except that only 20 iterations were used (since 60 iterations required considerable computer time); also c was fixed at 0.95. The results were examined for NO^+ lines even though the least-squares analysis of this region (Section 2.4) and the deconvolutions described above (Section 3.3) indicate that NO^+ was not observed by the FWI.

We elected to use scans 8, 6, 2 and the sum (coaddition) of scans 2, 3 and 4. Scans 8 and 6 were selected because they have little or none of what resembles a "continuum" component in most other scans. As pointed out by Pliva, et al (1980), a continuum can result in spurious, weak lines (similar to sidelobes) adjacent to the deconvolved emission lines. Scans 2, 3 and 4 were used because they were the basis for identification of NO^+ by USU.

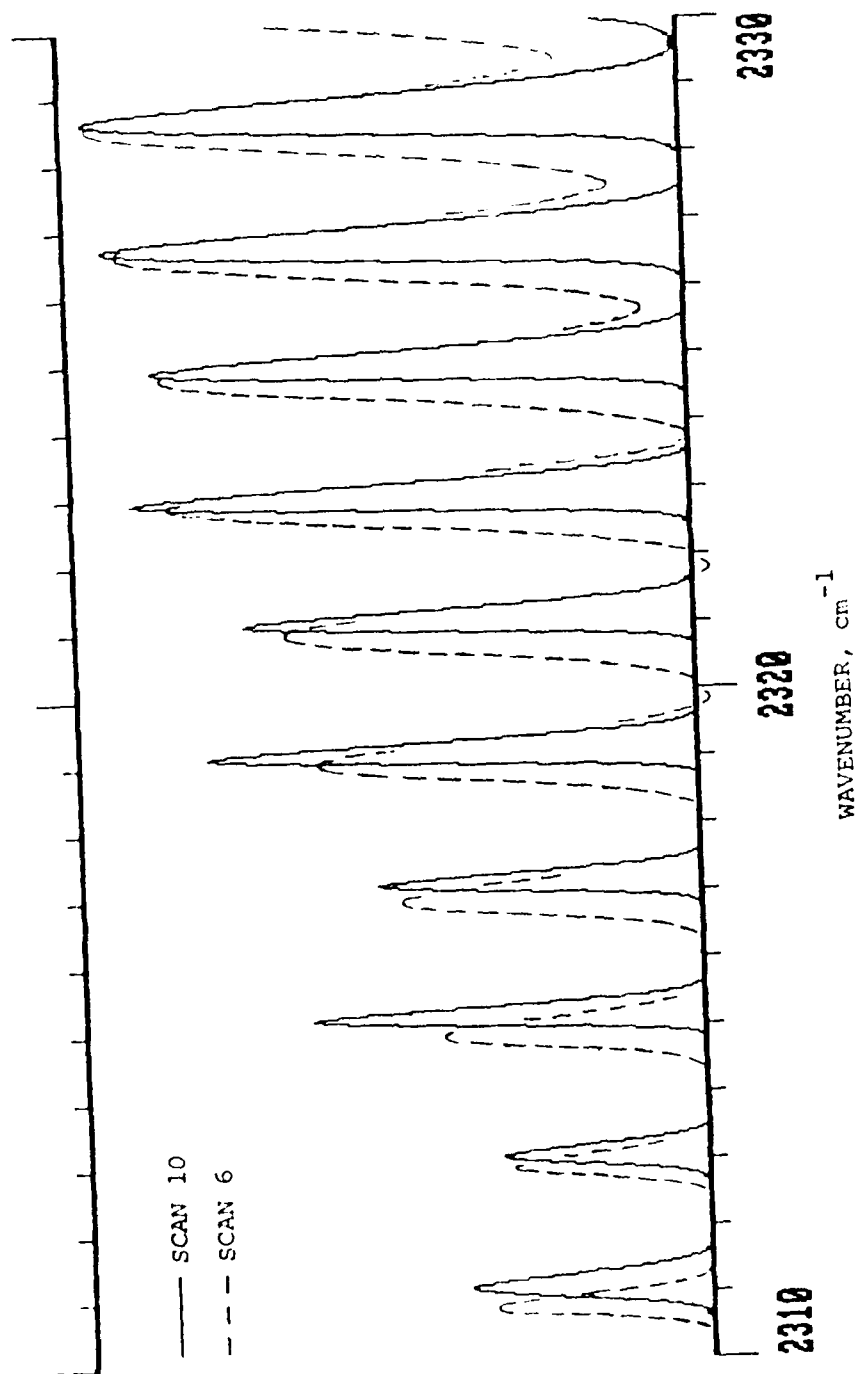


Figure 19. A comparison of the deconvolved spectra for scans 10 and 6. The latter appears shifted and stretched relative to the former.

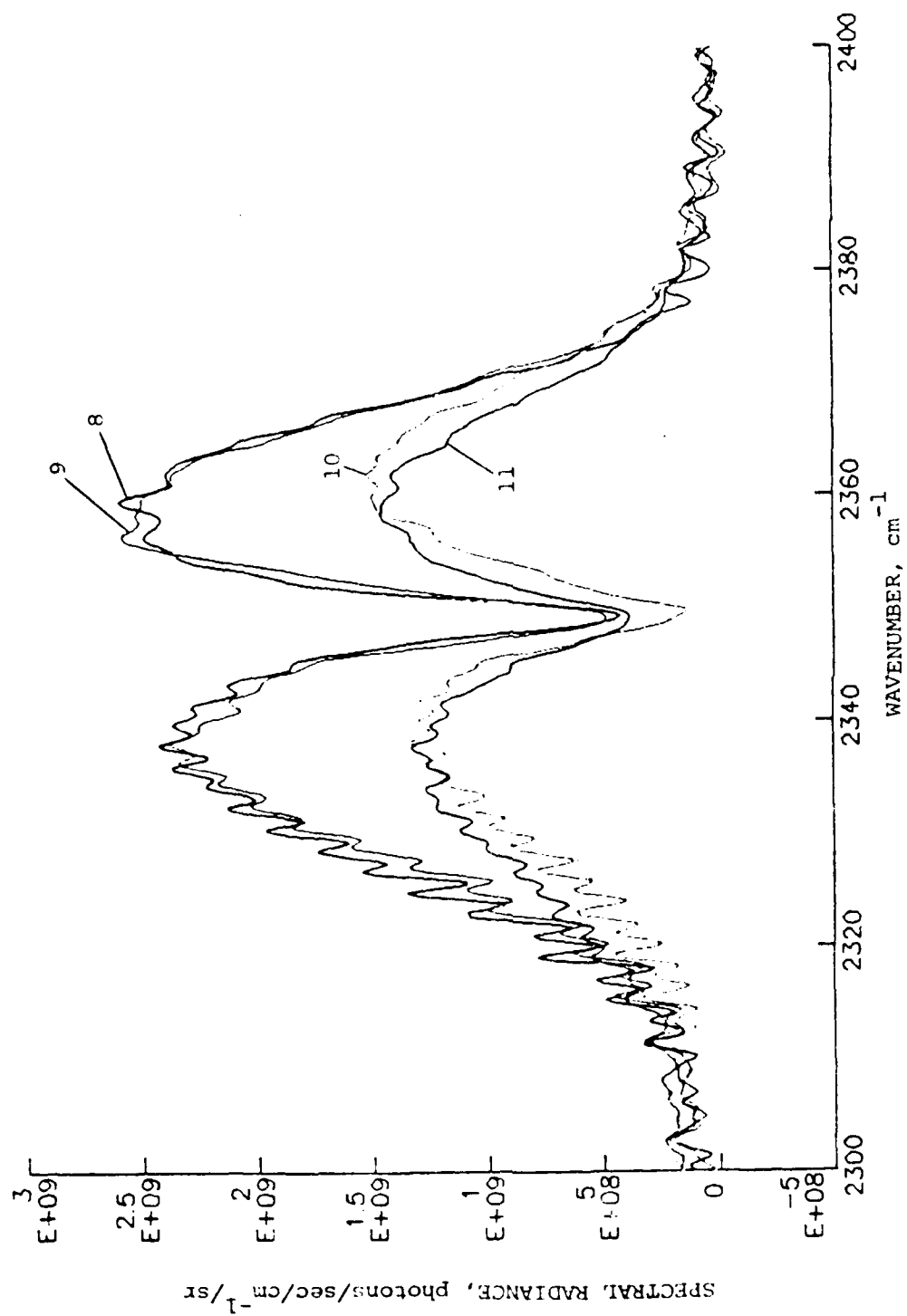


Figure 20. Spectra computed (by USU) from Hamming-apodized interferogram. Note the apparent wavenumber scale shift between scans 10 and 11.

Figures 21 through 24 show the deconvolution results for scans 8, 6, 2 and 2 + 3 + 4, respectively. An obvious visual feature of these spectra is their overall poor correlation with one another. Indeed, the initial (image) spectra exhibit a similar lack of correlation, as do the spectra computed by USU with Hamming apodization. There are, however, a few lines that appear consistently in the four spectra: the ones near 2233 cm^{-1} , 2252 cm^{-1} , 2258 cm^{-1} and the one just short of 2290 cm^{-1} .

Figure 25 shows the calculated locations of NO^+ lines with rotational quantum numbers up to ~ 20 in the $2220\text{--}2300\text{ cm}^{-1}$ region. Each of the bands 1-0 through 6-5 are represented by a displaced set of hash marks, and again by shorter hashes just above the wavenumber axis. J. Winick of AFGL provided the line positions as well as relative line strength estimates (not indicated in the figure) for an assumed rotational temperature. For this temperature, the strongest lines occur near $J = 7$ in the P branches and near $J = 5$ in the R branches. The strongest lines of each band are indicated by the emphasized hash marks.

A transparency of Fig. 25 was overlaid on the four deconvolution results (Figs. 21-24) to determine if the latter contain a significant number of the stronger NO^+ lines. The predicted positions of the P5 through P9 lines of the 2-1 band coincide with relative maxima in the deconvolved coadded spectrum (Fig. 24). However, there are few, if any, similar correlations in other parts of this spectrum, or in the other three cases, even if one allows for slight spectral shifts or scale stretching. Our conclusion is that NO^+ is not present or is masked by a stronger emitter(s).

Other common atmospheric species that radiate in the $2220\text{--}2300\text{ cm}^{-1}$ region are $\text{C}^{13}\text{O}_2^{16}$, N_2O and ozone. A cursory review of laboratory data, solar spectra and line atlases indicated that these molecules are not responsible for the observed emissions.

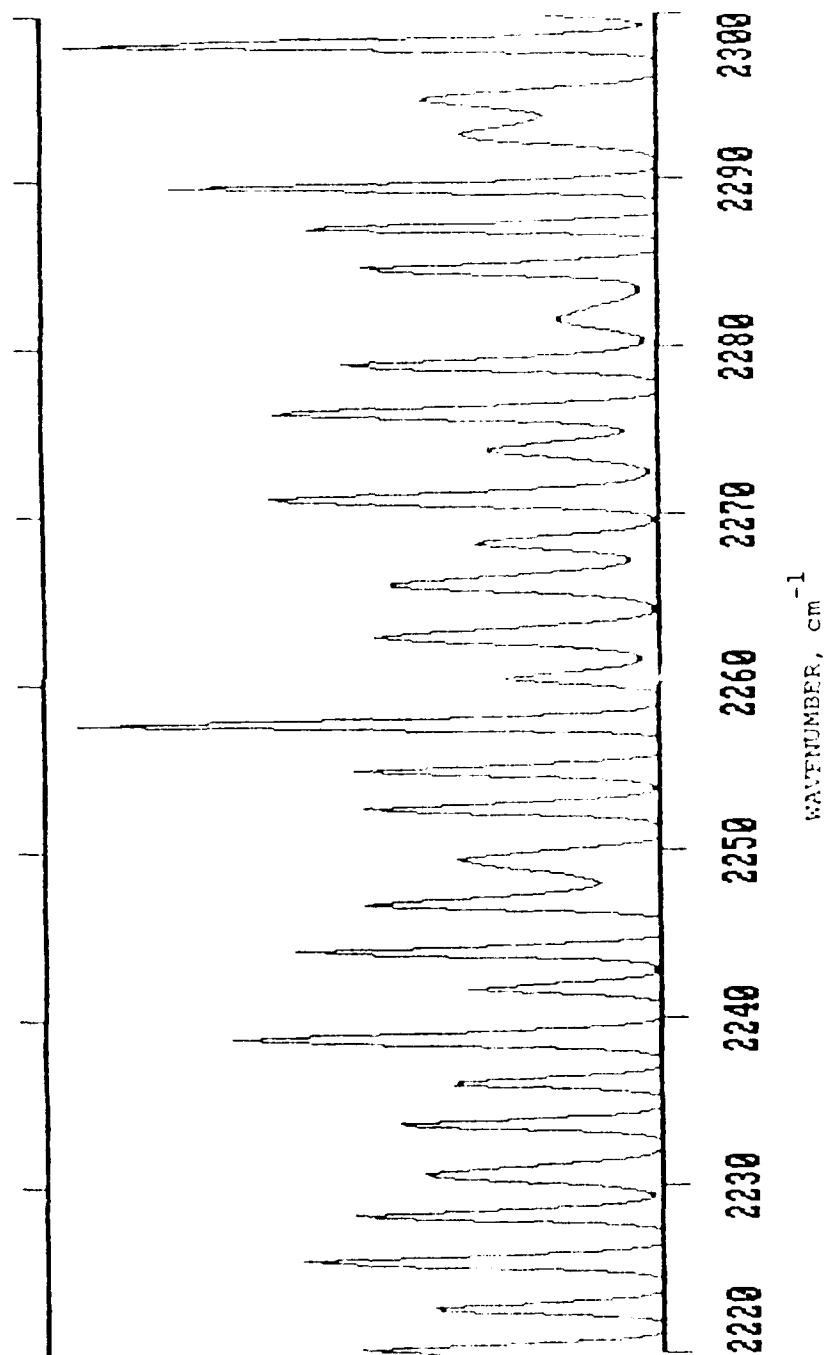


Figure 21. Deconvolved spectrum for scan 8.

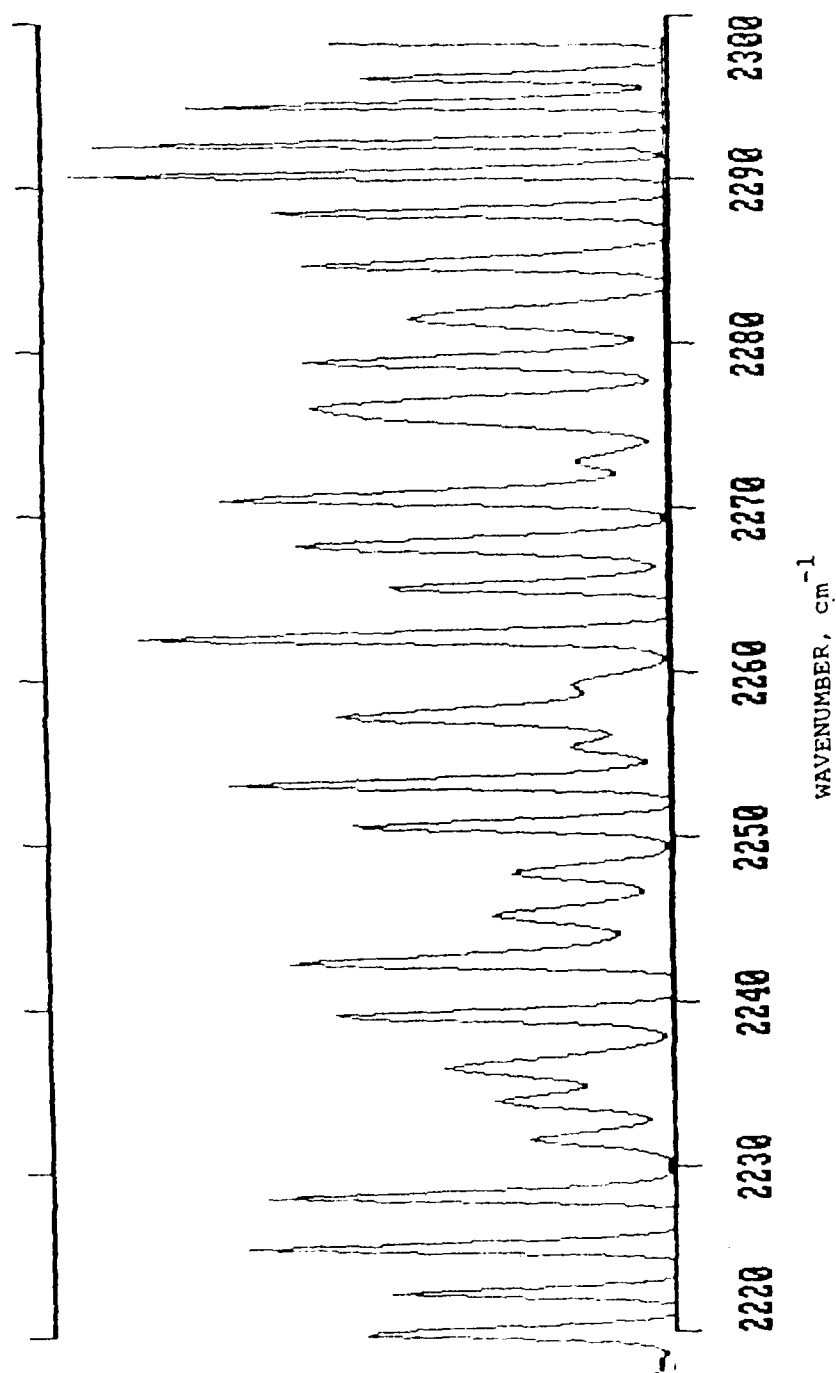


Figure 22. Deconvolved spectrum for scan 6.

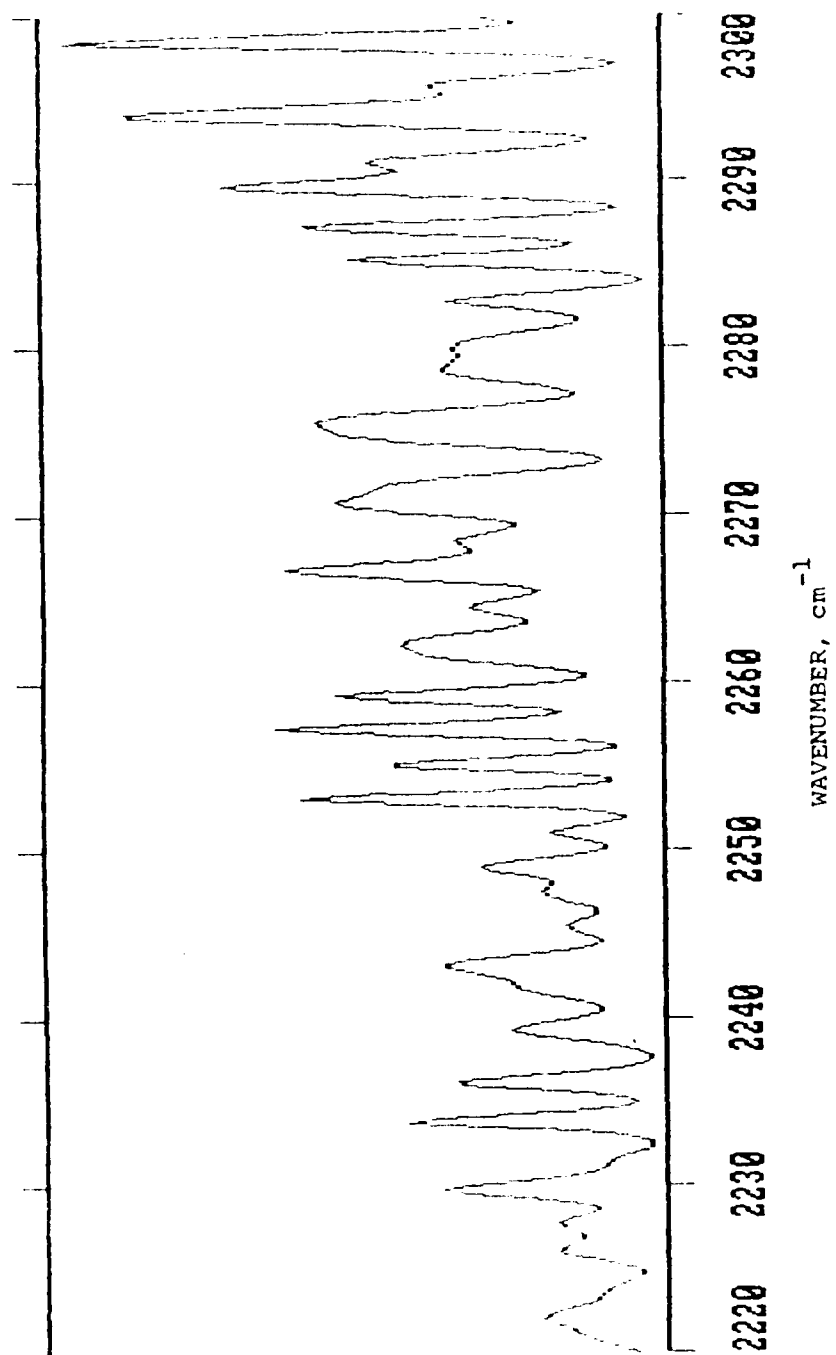


Figure 23. Deconvolved spectrum for scan 2.

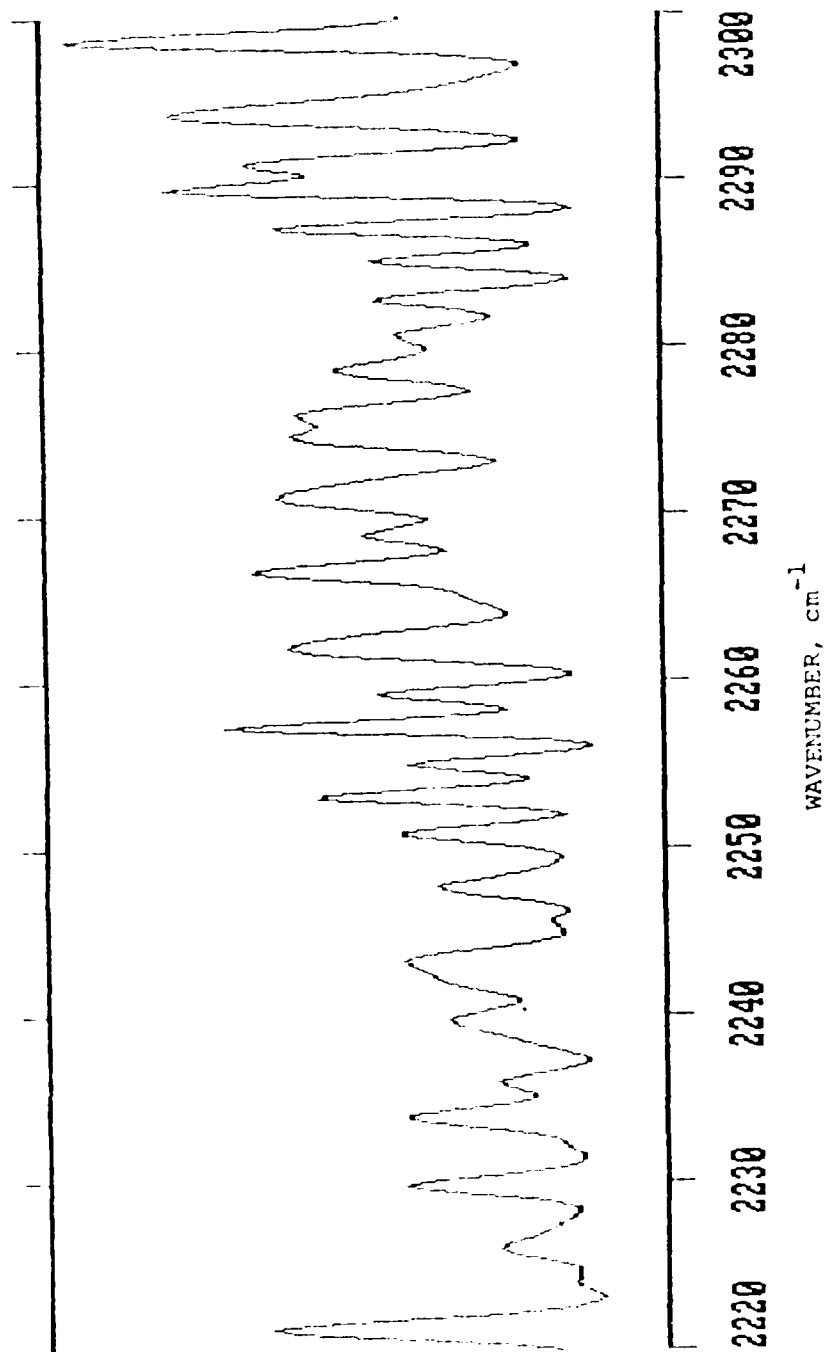


Figure 24. Deconvolved spectrum for coadded scans 2, 3 and 4.

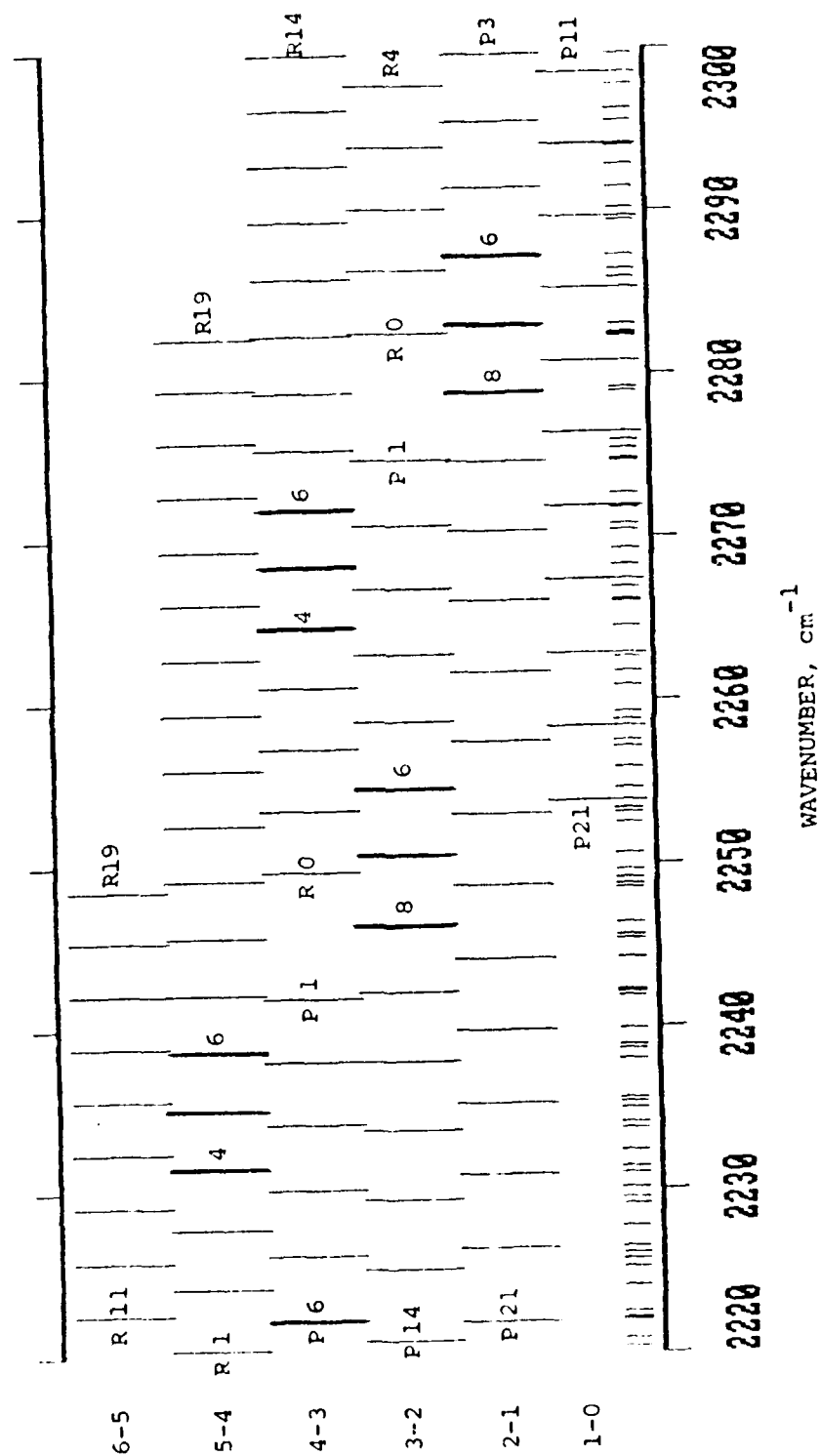


Figure 25. Positions of NO⁺ in 2220-2300 cm⁻¹ region.

We have one reservation that should be stated regarding the deconvolution results for the $2220\text{-}2300\text{ cm}^{-1}$ region. The signal-to-noise for this region is estimated to be only ~ 45 . Pliva, et al (1980), in deconvolving Doppler-limited spectra, state that when their signal-to-noise was reduced to 100 they could "reliably deconvolve only to a resolution enhancement factor of 2-2.5 before objectionable noise begins to appear on the deconvolved curve". Our results may contain artifacts due to the relatively low signal-to-noise. On the other hand, the scan-to-scan nonreproducibility of the image spectra suggests that instrumental artifacts may dominate the spectrum in low signal-to-noise regions.

REFERENCES

- Steed, A., J. C. Ulwick, C. Harris, F. Cook and R. Straka, "Rocket-borne Interferometer Measurement of SWIR/MWIR Spectra", EOS Trans. AGU, 64, 784, 1983.
- Jansson, P. A. (Editor), *Deconvolution with Applications in Spectroscopy*, Academic Press, New York, 1984.
- Pliva, J., A. S. Pine and P. D. Wilson, Appl. Opt., 19, 1833 (1980).
- Rothman, L. S., A. Goldman, J. R. Gillis, R. R. Gamache, H. M. Pickett, R. L. Poynter, N. Husson and A. Chedin, Appl. Opt., 22, 1616 (1983).
- Sharma, R. D., R. D. Siani, M. K. Bullitt and P. O. Wintersteiner, "A Computer Code to Calculate Emission and Transmission of Infrared Radiation Through Non-Equilibrium Atmospheres", AFGL-TR-83-0168, AD137162, Air Force Geophysics Laboratory, Hanscom AFB, Massachusetts 01731, 1983.
- Zachor, A. S. and R. D. Sharma, "Retrieval of Non-LTE Vertical Structure from a Spectrally Resolved IR Limb Radiance Profile", J. Geophys. Res., A, to be published in January 1985 (Paper 4A8044).

END
DTIC
FILMED
4-86